Effects of carbon impurities on the power radiation and tungsten target erosion in EAST

Chaofeng Sang, Rui Ding, Xavier Bonnin, et al.

View Online   Export Citation   CrossMark

ARTICLES YOU MAY BE INTERESTED IN

Divertor plasma detachment
Physics of Plasmas **23**, 055602 (2016); https://doi.org/10.1063/1.4948273

The effects of particle recycling on the divertor plasma: A particle-in-cell with Monte Carlo collision simulation
Physics of Plasmas **25**, 052507 (2018); https://doi.org/10.1063/1.5023731

Experimental investigation and SOLPS-ITER modeling of Ne-seeded radiative divertor H-modes plasma on EAST
Physics of Plasmas **26**, 052501 (2019); https://doi.org/10.1063/1.5085892

Effects of carbon impurities on the power radiation and tungsten target erosion in EAST

Chaofeng Sang,[1,a)] Rui Ding,[2] Xavier Bonnin,[3] Liang Wang,[1,2] Dezhen Wang,[1] and EAST Team

[1]*Key Laboratory of Materials Modification by Laser, Ion and Electron Beams (Ministry of Education), School of Physics, Dalian University of Technology, Dalian 116024, China*
[2]*Institute of Plasma Physics, Chinese Academy of Sciences, Hefei 230031, China*
[3]*ITER Organization, Route de Vinon-sur-Verdon, CS 90 046, F-13067 St-Paul-lez-Durance Cedex, France*

Tungsten (W) and Carbon (C) are, respectively, used as the plasma-facing materials for upper and lower divertors in EAST. This provides an opportunity to study the plasma performance with both W and C divertors simultaneously. In this work, simulations are carried out by using the edge fluid-plasma/kinetic-neutral code SOLPS5.0-EIRENE99, with emphasis on the C impurity transport and its effect on the power radiation and erosion of the upper W divertor target. Three typical magnetic field equilibrium configurations, i.e., lower single null, upper single null (USN), and double null (DN), are studied. The main deuterium (D) plasma and C impurities at each ionization state and their neutrals are considered in the simulation. The SOLPS output such as averaged incident ion energy and particle flux density of each species are used to calculate the erosion rate of W walls using the empirical formula for physical sputtering yield. The transport and performance of C impurities on different plasma conditions of each configuration are investigated by changing the C source strength and upstream plasma density. The upper W target erosion by C ions under different conditions is also evaluated. The simulation results indicate that (1) carbon is a strong radiator in EAST divertor temperatures of 10–20 eV; (2) the amount of carbon transported from the lower carbon divertor to the upper tungsten divertor in both USN and DN configurations is predicted to be too small to cause significant W sputtering; and (3) C^{6+} dominates upper W erosion in the DN case. © 2018 Author(s). All article content, except where otherwise noted, is licensed under a Creative Commons Attribution (CC BY) license (http://creativecommons.org/licenses/by/4.0/).
https://doi.org/10.1063/1.5038848

I. INTRODUCTION

The divertor, which is designed to handle particle and energy exhaust from the core plasma and impurity screening, is the main region for the plasma-surface interactions (PSI) in a tokamak.[1] Divertor plasma-facing components (PFCs) are put in place to provide adequate protection of in-vessel structures, sufficient heat exhaust capability and to be compatible with the requirements of plasma purity.[2] Control of heat flux and material erosion at divertor target plates is a major issue for design and operation of next-step high-power steady-state fusion devices. This necessitates the achievement of highly dissipative or detached divertor conditions to maintain both the heat flux below 10 MW/m² and plasma electron temperature below 5 eV to suppress sputtering at the divertor surface.[3–7]

Carbon (C) and tungsten (W) are used as the main PFCs in most existing fusion devices. C-PFCs are chosen mainly due to their high thermal shock resistance and tolerance to off-normal events (ELMs, disruptions) without melting.[1,8] However, the C-PFCs suffer from strong erosion due to not only physical sputtering, but also chemical erosion, which is strong even at low plasma edge temperature.[9] Therefore, the

lifetime of C wall may be greatly reduced. Moreover, the tritium retention is a big challenge for C wall during deuterium-tritium discharges.[10–13] The high-Z material W is a promising candidate of the PFCs for the future tokamak reactors, such as International Thermonuclear Experimental Reactor (ITER),[14] Chinese Fusion Engineering Test Reactor (CFETR),[15] Fusion Nuclear Science Facility (FNSF),[16] and European Demonstration Fusion Power Plant (EU-DEMO),[17] due to its high melting point (3683 K), low tritium retention, and low sputtering yield.[18,19] However, as a high-Z material, the bremsstrahlung radiation of W is very high at the core plasma, and even a small fraction of W impurities (10^{-5}) will extinguish the fusion reaction.[1,20] The off-normal events and the other impurities (such as C, Be) would make it much worse.[21–26] Thus, it is important to investigate the erosion of W PFCs in fusion devices.

The Experimental Advanced Superconducting Tokamak (EAST) is a fully superconducting divertor tokamak with D-shaped poloidal cross-section, advanced divertor configuration, and heating scheme similar to ITER, aiming at high-performance plasma for long-pulse operation. The main parameters of the device are: the major radius $R = 1.7$–1.9 m, minor radius $a = 0.4$–0.45 m, elongation $\kappa = 1.2$–2.0, plasma current $I_p \sim 1$ MA, toroidal field $B_T = 3.5$ T, and expected plasma pulse length up to 1000 s.[27–29] The machine

a)Author to whom correspondence should be addressed: sang@dlut.edu.cn

can be operated in lower single null (LSN), double null (DN), and upper single null (USN) divertor configurations, which can be flexibly switched during a long-pulse discharge. Low impurity generation and fuel retention, high particle, and heat flux removal capacities are key issues for high performance and long pulse plasma discharges on EAST.[30] The upper divertor of EAST has been upgraded to ITER-like tungsten monoblock configuration in 2014 (Refs. 29 and 30) to handle the heat flux up to $10\,\mathrm{MW/m^2}$ for steady state and $15\,\mathrm{MW/m^2}$ for transients events.[31,32] This can provide important information for the PFC development of the further devices.

At present, W and C are, respectively, used as upper and lower divertors on EAST. This provides us a great opportunity to study the plasma performance on both W and C divertors simultaneously. On the one hand, C is easily eroded by the incident deuterium (D) plasma, and C impurities, as a good radiator in the divertor region, could help to achieve plasma detachment.[33,34] On the other hand, the low erosion rate of the W can be greatly enhanced due to the higher W sputtering yield by impurities, resulting in an unexpected high-Z content in the core plasma.[19,22,35,36] Therefore, two issues need to be assessed simultaneously.

1. The effects of carbon on the detachment, with the emphases on C impurities transport and the power radiation by C impurities.
2. The potential impact of C impurities from the lower divertor on the erosion of the upper W divertor.

Two-dimensional codes have been subjected to significant code validation efforts and they are extensively used for both interpretative and predictive modelling of the edge plasma in various tokamaks.[37–47] In this work, we present detailed modeling studies of effect of C impurities on the power dissipation in the divertor/scrape-off layer (SOL) region and the erosion of the W upper divertor by the C created at lower divertor in EAST, by using the Scrape-Off Layer Plasma Simulation (SOLPS) code (SOLPS5.0/EIRENE99). In Sec. II, a brief description of the SOLPS code package and modeling setup for EAST are given. In Sec. III, the transport of C and power radiated by C for LSN, USN, and DN magnetic field equilibrium configurations are systematically studied. The upper W target erosion by C impurities is also assessed. The conclusions and discussions are summarized in Sec. IV.

II. SIMULATION MODEL

In this work, the SOLPS5.0/EIRENE99 code package, a coupled version of the multi-fluid transport code B2.5[48] and the kinetic neutral transport code EIRENE (1999 version),[49] is applied for the modeling study, with fuel D. The electrons and ions for both D and C at each ionization state are handled by the B2.5 code,[48] while the neutrals (D, C and D_2) are tracked by the EIRENE code,[50] in which ionization, charge exchange, dissociation, elastic collision, and recombination processes are taken into account. B2.5 is written in a curvilinear orthogonal coordinate system. It has two dimensions: poloidal coordinate and radial coordinate orthogonal to the flux surface.[48] B2.5 solves a set of continuity and parallel

momentum equations for each ion species, and energy equations for calculating the ion temperature T_i and electron temperature T_e. EIRENE solves a set of linear transport equations for the neutral atoms and molecules including different collision processes. In the current simulations, the input power at the core boundary of the modeling grid is fixed to $P_{SOL} = 1.5\,\mathrm{MW}$ unless otherwise stated, divided equally between ions and electrons. The D^+ density at the innermost boundary [e.g., r-r_{sep} at outer mid-plane (OMP) $\sim -6.6\,\mathrm{cm}$, LSN magnetic field configuration] is fixed, ranging from 2.0 to $7.0 \times 10^{19}\,\mathrm{m^{-3}}$ (n_e at the separatrix of OMP ~ 0.9 to $3.3 \times 10^{19}\,\mathrm{m^{-3}}$). The fluxes of other ions and neutrals are assumed to be zero at this innermost boundary. The leakage boundary condition at the scrape-off layer& private flux region, $\Gamma = \alpha c_s n_i$, is used, where c_s is the sound speed, n_i is the particle density, *and* α is the leakage factor (assumed here 10^{-3}). The standard sheath boundary condition at the target is applied: for the momentum equation, a strict Bohm criterion, mach number (M) = 1 flow at the plasma–sheath boundary is enforced for the parallel fluid velocity; for the density, zero gradient is used; for the energy, the parallel heat flux is computed as $\gamma \Gamma T$ (for both ions and electrons). These boundary conditions are the same as in Refs. 41 and 43.

When ions hit the wall, a part of them are reflected as recycling neutrals and sent back into the simulation domain. There are two parts of the recycled particles: reflected D atom and thermal release D_2, and the total particle recycling rate (R) is fixed. The particle reflection rate (R_D) is determined by the TRIM database, see Ref. 49 for details. The rest of the recycled particles are D_2 molecules via thermal release. The impact of the particle recycling/reflection on the divertor plasma has been studied in recent work by PIC-MCC simulation.[51] The wall temperature is assumed to be $0.026\,\mathrm{eV}$. In the simulation since the chemical sputtering yield is fixed, the wall temperature only affects the particle reflection/recycling. The recycling rate for D species is set to 1.0 (except at the pump entrance), 0.0 for carbon neutrals/ions.[52] Four pumps are set at the corner of each divertor with the recycling rate 0.8. Neither gas puffing nor electromagnetic drifts are considered in the simulation. Apart from deuterium plasma species (D^0, D_2^0, D^+, D_2^+), different C impurity species are also taken into account (C^0, C^+, C^{2+}, C^{3+}, C^{4+}, C^{5+}, C^{6+}). The considered reactions such as ionization, charge exchange, dissociation, elastic collisions, and volume recombination processes are listed in Ref. 53.The radial transport coefficients are chosen as follows: particle transport coefficient $D_\perp = 0.8\,\mathrm{m^2 s^{-1}}$ and electron and ion heat conductivity coefficients $\chi_{\perp,e} = \chi_{\perp,i} = 1.7\,\mathrm{m^2 s^{-1}}$ for all the particles. To simulate the electron density drop across the pedestal for H-mode, a radial transport barrier is imposed by reducing $D_\perp = 0.1\,\mathrm{m^2 s^{-1}}$ in the pedestal region; $D_\perp = 1.0\,\mathrm{m^2 s^{-1}}$ and $\chi_{\perp,e} = \chi_{\perp,i} = 1.0\,\mathrm{m^2 s^{-1}}$ at the outer SOL, which are the same as the previous EAST simulations.[41,54] Only steady-state conditions are simulated, and the condition during ELMs is not considered. The radiated power is calculated by including the line and bremsstrahlung radiations for both ions and neutrals. The total power flux to the target is calculated by summing the contributions from electrons,

ions, and recombination processes (ion particles hit the target and recombine to neutrals).

EAST has gone through four generations of PFCs since the first plasma in 2006.[30] Currently, it has a graphite lower divertor target and W upper divertor target as shown in Fig. 1, while the main chamber PFCs (first wall) are molybdenum. In the simulations, for the graphite PFCs, the physical sputtering yield Y_{phys} is calculated by the modified Roth-Bohdansky formula,[9] while the chemical sputtering yield is fixed with spatially the same value (varies from 0.0 to 0.1). For the other PFCs, no C is sputtered out. Since it is a great challenge for SOLPS to directly simulate the high-Z impurities transport by using the B2-Eirene coupled code, we do not trace the trajectory of high-Z impurities in this paper. Several W transport simulations have been done only using SOLPS with the fluid-neutral model, see Refs. 55 and 56.

In this paper, three typical magnetic field configurations of EAST, i.e., LSN, USN, DN, created by EFIT[57] with normal B_t direction (the direction of $B \times \nabla B$ points to the lower divertor), are used, as shown in Fig. 2. The number of cells in the computational domain is 96 in the poloidal direction and 36 in the radial direction. A series of simulations have already been successfully done by SOLPS[44–46,58,59] for various tokamak devices. Since there are too limited experimental data and more impurities than C (for example, Si, Li) in EAST, a direct code-experiment benchmark was not made in the present work. We focus on the analysis of the outer

divertor target. The inner divertor is still included in the simulations, but no additional effort is made for further data analysis to avoid any confusion.

III. SIMULATION RESULTS

A. The lower single null case

LSN magnetic field equilibrium (see Fig. 2 for the simulation mesh) is selected to study the transport of C impurities and its effects on the plasma detachment. Chemical sputtering is the dominant erosion process of C. In the simulation, the chemical sputtering yield ($Y_{C,chem}$) is fixed. A scan with the $Y_{C,chem}$ varies from 0.01 to 0.1 has been done to check its impact on the plasma solution. Figure 3 shows the radial profiles of different quantities at the outer mid-plane (OMP) and lower outer target (LOT) with different $Y_{C,chem}$. It can be seen that the C impurities do not affect the upstream plasma condition significantly since their densities are very low compared to the main plasma (the total C density at the core-edge interface is only 3.0 to 5.5×10^{17} m^{-3}), as shown in Fig. 3(a3). However, at the LOT, the C impurities play an important role. It appears that the enhanced wall C source leads to strong energy radiation in the divertor region, significantly reducing the electron temperature and power flux density to the LOT, similar to Refs. 33 and 34. As the $Y_{C,chem}$ increases from 0.01 to 0.1, the total peak C density at the LOT increases from 0.2 to 1.4×10^{19} m^{-3}, the ratio of n_{ct} and n_{et} could achieve as high as 14%. The electron density also increases as T_e decreases.

As shown in Fig. 3, C densities at both OMP and LOT increase with C source strength ($Y_{C,chem}$). Since the lower graphite target is the only C source (shown in Fig. 1), the C density at the outer target is two orders of magnitude higher than that at OMP. Figure 4 shows the 2D contour of total C density and T_e with different $Y_{C,chem}$ (0.01, 0.05, 0.1), and the corresponding target profiles. It appears that most of the C impurities distribute in the lower divertor region, with the C$^+$ and C^{2+} being the main charge states. However, the carbon fraction (n_C/n_e) in the divertor region can be smaller than that in the upstream SOL region, due to the fact that the divertor has a factor of two higher plasma density. As we increase the $Y_{C,chem}$, the C density is greatly enhanced. One of the interesting observations is that the peak C density appears in the inner divertor. This is mainly due to the divertor in-out asymmetries during the operation, which means that T_e at the inner target is lower than that at the outer target. As a result, the direction of the particle flux is from the outer target to inner target to maintain the plasma pressure balance ($P = n_e T_e + \sum_i n_i T_i$). Therefore, both electron density and C density at the inner divertor are higher than those at the outer divertor, even though the particle fluxes to the outer target are higher than those to the inner target (this means that the C source at the outer target is stronger than that at the inner target). The T_e contour in Fig. 4(b) clearly shows that as the C density increases, T_e at the target decreases dramatically, indicating that C could help to achieve plasma detachment at a lower upstream plasma density. It should be noted that the cross-field drifts[60,61] are not included due to numerical difficulties, even
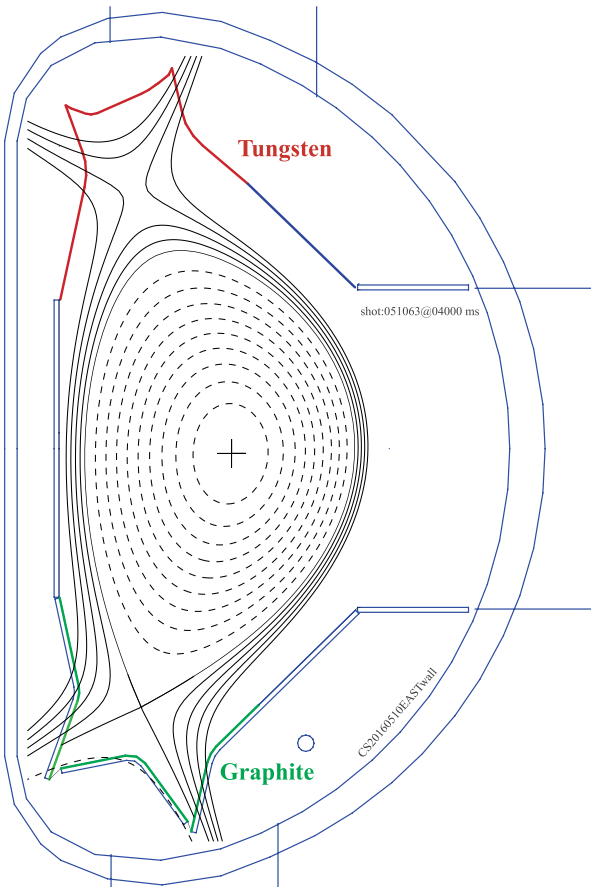

FIG. 1. The poloidal view of the invessel wall structure and the PFCs of EAST. The lower target is made out of graphite, the upper target is in tungsten, and the rest of the PFCs are in molybdenum.
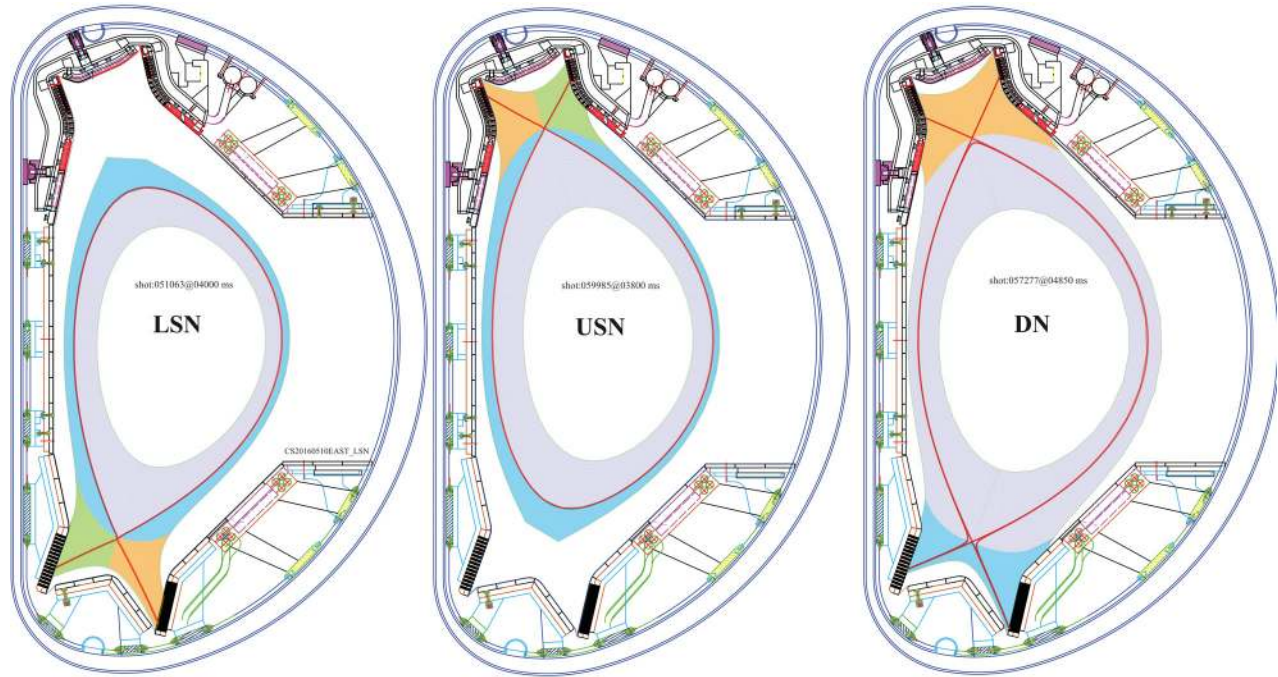
FIG. 2. The meshes for three magnetic field configurations (LSN, USN, DN) used in the simulations. The color is used to define the regions (Core, target, SOL, etc.) of the simulation domain to calculate the radiated power.

though some other code simulations indicated that the drifts play an important role in the particle transport.[52,62,63]

The peak T_{et}, q_t, and Γ_t at the outer target as functions of $Y_{C,chem}$ are shown in Fig. 5(a). It can be seen that the peak T_{et} decreases from 41 eV to 7.5 eV and q_t decreases from 3.6 MW/m^2 to 0.8 MW/m^2, while $Y_{C,chem}$ increases from 0.01 to 0.1. Again, this is the evidence that C could help to

dissipate energy as well as to achieve plasma detachment. To discuss the radiated power, we divide the simulation domain into three parts: (1) core+SOL, region above the divertor entrance, (2) inner target, from the inner divertor entrance to the inner target, and (3) outer target, from the outer divertor entrance to the outer target, as shown in Fig. 2 in different color representing different regions. Figure 5(b)
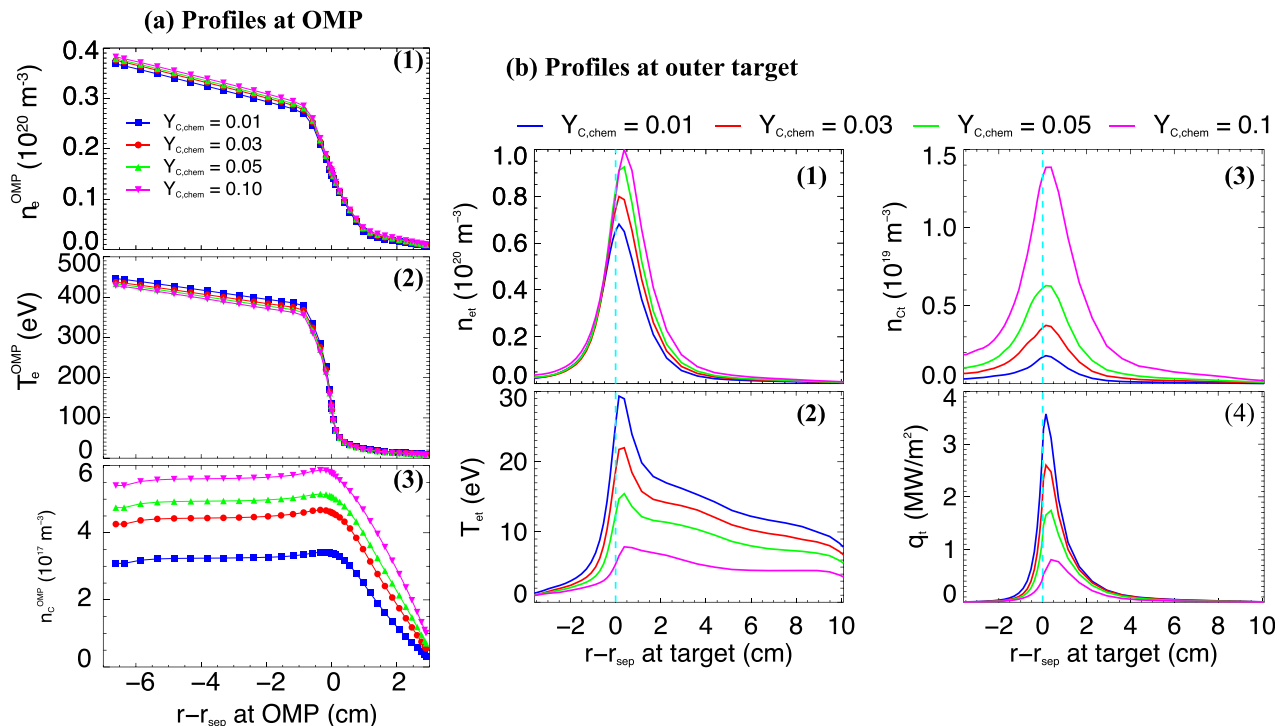

FIG. 3. The radial profiles at the OMP (a1) electron density n_e, (a2) electron temperature T_e, (a3) the total C density n_c, i.e., the sum of all the charge states of C impurities; and the profiles at the LOT (b1) electron density n_{et}, (b2) electron temperature T_{et}, (b3) the total C density n_{ct}, (b4) the actual total incident energy flux density q_t, with different chemical sputtering yields of the graphite wall ($Y_{C,chem} = 0.01, 0.03, 0.05, 0.1$).
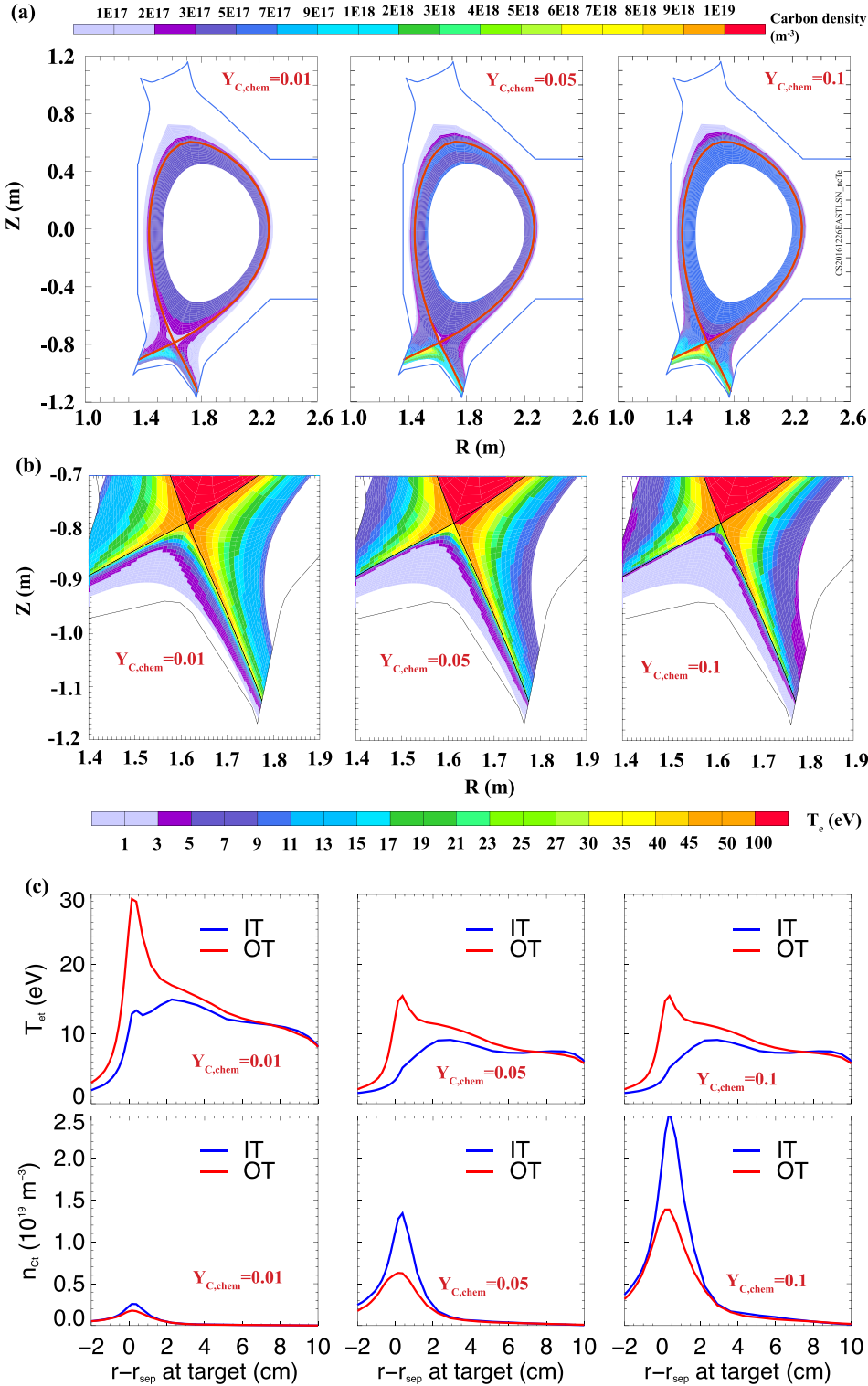
FIG. 4. The 2D contours of (a) total carbon density n_c and (b) electron temperature T_e, with different chemical sputtering yields of the graphite wall ($Y_{C,chem} = 0.01, 0.05, 0.1$); (c) the corresponding T_e and n_c profiles at inner target (IT) and outer target (OT).

shows the total radiated power and C radiation in different regions as functions of $Y_{C,chem}$. The ratio of power radiated by C increases from 68% to 91% as $Y_{C,chem}$ increases from 0.01 to 0.1, indicating that C is a very good power radiator, and this is the reason why tokamaks with full metal-PFCs need N_2 seeding (which is a similar energy radiator to C) to dissipate power.[64] For the total radiated power, the divertor (both inner and outer divertor) radiation contribution is about 90%, and the rest is radiated in the SOL&Core region of the simulation domain.

2D fluid codes such as SOLPS, UEDGE,[65] and EDGE2D-EIRENE[66,67] have been widely used for modelling of edge tokamak plasmas of carbon devices. SOLPS modeling of ASDEX Upgrade edge plasmas[37,58] showed that the radiated power depends strongly on the choice of the chemical sputtering coefficient, and the radiation was nearly equally split between deuterium and carbon impurities when $Y_{C,chem} = 0.015$. However, the simulated CIII emission was below the experimental one by at least a factor of 2. The other SOLPS modeling of ASDEX Upgrade indicated that high
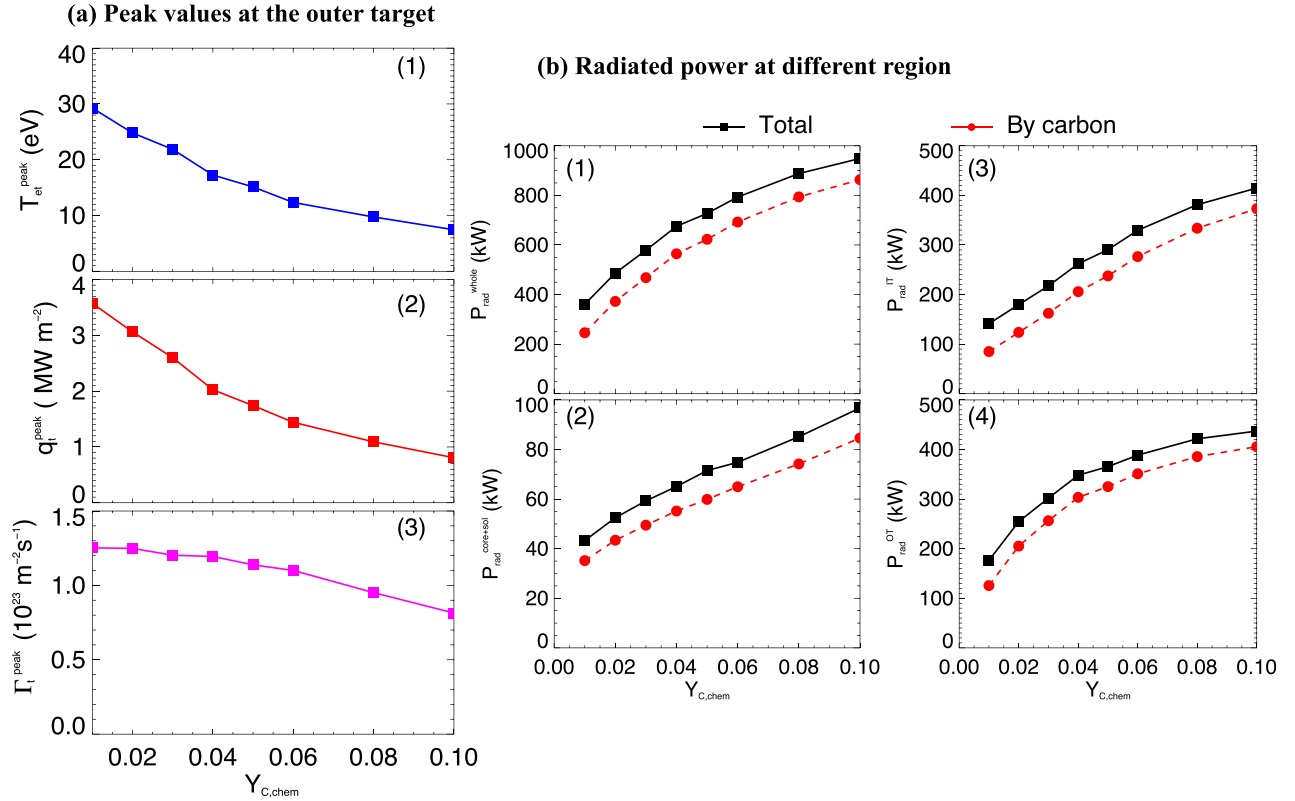
FIG. 5. The peak plasma values at the LOT (a1) T_{et}, (a2) q_t, (a3) Γ_t; and the total and C radiated power in (b1) total simulation domain, (b2) core and SOL region, (b3) the inner divertor region, and (b4) the outer divertor region, as functions of $Y_{C,chem}$.

values of Y_{chem} (> 0.2) were not supported by experimental observations,[33] and $Y_{chem} = 0.1$ was applied. With the change from JET-C to JET-ILW, a factor of 2–4 reduction in the divertor radiated power and 25%–50% increase in the power deposited to the outer plate was predicted by EDGE2D-EIRENE,[42,68] indicating that carbon is a good power radiator. SOLPS modeling of well-diagnosed DIII-D experiments[45] showed that $Y_{C,chem} = 0.01$, 0.02 is sufficient for DIII-D L-mode discharge; however, significant radiation shortfall has been observed, especially for high density plasma. SOLPS modeling of MAST/MAST-U also illustrated that C is a very good radiator in the typical divertor temperatures of 10–20 eV.[46] UEDGE modeling of DIII-D discharge indicated that approximately 86% of the radiated power arises from carbon impurities radiation.[69] UEDGE modeling of DIII-D, AUG, and JET presented that chemical sputtering yields of 3%–4% move the numerical solutions closer to many of the measurements.[70] These simulation results by different codes are quantitatively consistent with our results. The dominant sputtering mechanism for carbon sources is chemical sputtering.[52] Different simulations indicate that the chemical sputtering yield depends on different devices or different discharge conditions, varying from 0.01 to 0.1.

B. The upper single null case

In this subsection, the USN case is simulated; see the computational grid in Fig. 2. For the USN configuration, the plasma only contacts the upper W divertor, and only neutrals traced by EIRENE can reach the lower graphite divertor.

Therefore, all the C impurity sources are from lower target, created by the neutrals hitting the graphite wall. Density scans without and with C sputtering ($Y_{C,chem} = 0.01$) cases have been done. Figure 6(a) shows the peak and OSP T_{et}, q_t, and Γ_t at the upper outer target (UOT) as functions of $n_{e,sep}^{OMP}$. It can be seen that as the upstream density increases, T_{et} and q_t fall significantly. While raising the upstream density, it is observed that Γ_t increases continually. The detachment is defined to occur when Γ_t rolls over;[71–74] thus, the high density solutions are close to the onset of partial detachment. In contrast to the LSN case, C has only slight impact on the upper divertor plasma solution. Figure 6(b) shows the radiated power as functions of $n_{e,sep}^{OMP}$ for both cases. Clearly, we can see that the power radiated by C in the upper divertor region is smaller than the total radiated power. Only in the core+SOL region, the power radiated by C is significant. However, since the divertor region contributes most of the radiated power, the fraction of power radiated by C in the whole simulation domain is very small. This is the main reason for the slight effect of C on the divertor plasma solution in the USN configuration.

The effect of C impurities on the plasma solution is determined by the C density and distribution. Figure 7(a) shows the C density profiles at the OMP and UOT for different $n_{e,sep}^{OMP}$ with $Y_{C,chem} = 0.01$. It can be seen that, as the plasma density increases, n_c at the OMP changes slightly and n_c at the UOT decreases. The reason can be attributed to the fact that higher upstream density could reduce T_e (both upstream and downstream, since the P_{SOL} is fixed); therefore, the transport of C can be suppressed due to smaller

(a) Values at the outer target
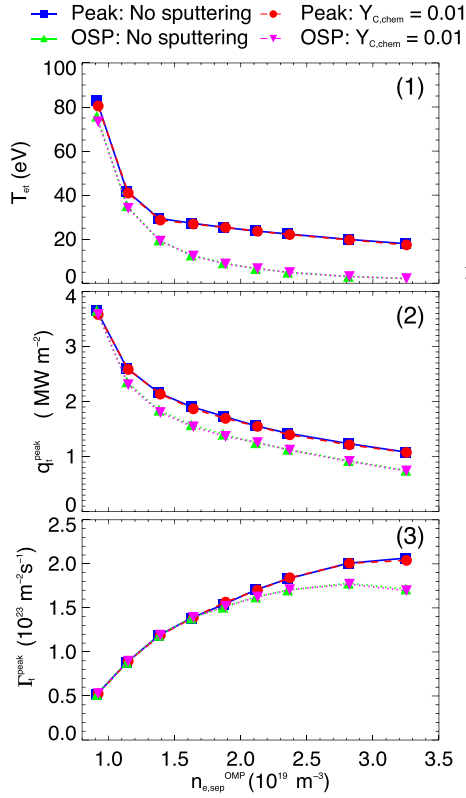
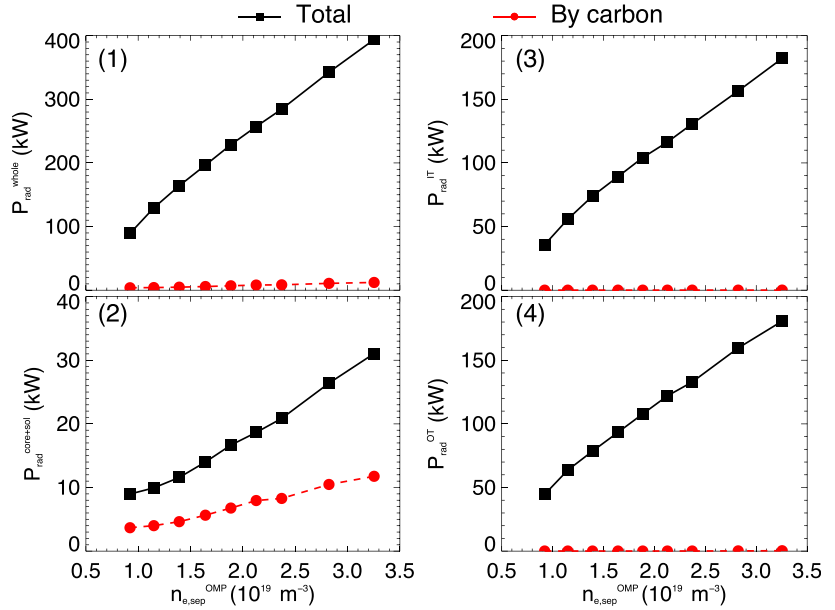**(b) Radiated power at different region**

FIG. 6. The peak and outer strike point values at the UOT (a1) T_{et}, (a2) q_t, (a3) Γ_t; and the total and carbon radiated power in, (b1) total simulation domain, (b2) core and SOL region, (b3) the inner divertor region, and (b4) the outer divertor region, as functions of $n_{e,sep}^{OMP}$.

parallel velocities of the impurities toward the targets, resulting in less C impurities reaching the UOT. It should be noted that the n_c density at the OMP is about one order of magnitude higher than that at the UOT. The upstream profiles of the total carbon density may be affected by the transport coefficients, which is beyond the scope of this work, see Refs. 47 and 75 for details. Figure 7(b) shows the 2D contour of n_c distribution for the density $n_{e,sep}^{OMP} = 1.6 \times 10^{19}$ m^{-3}. Since the lower target is the only C source (see Fig. 1), the

highest n_c is located near the lower target, and C impurities transport both inside (higher charge state ions) and outside (lower charge state ions) the separatrix. It is also noted that the C can hardly reach the upper target (both inner and outer), especially the private flux region. The peak n_c at the UOT appears far from the strike point.

The PFCs of the EAST upper divertor are the W monoblock as shown in Fig. 1. It is important to understand the W erosion with the presence of C impurities. Various models
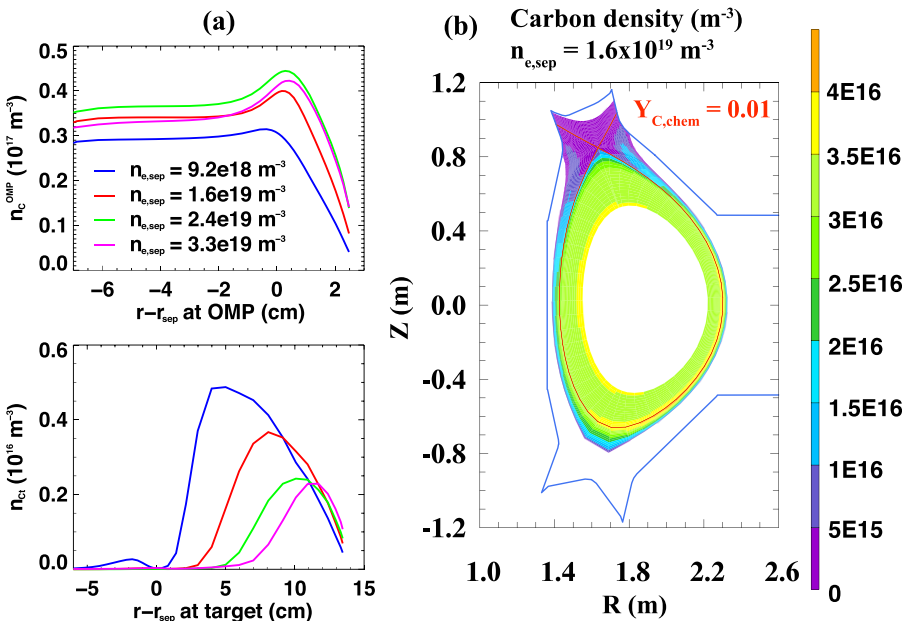

FIG. 7. (a) The radial profiles of n_c at the OMP and UOT for different upstream densities; (b) the 2D contour of n_c for the density $n_{e,sep}^{OMP} = 1.6 \times 10^{19}$ m^{-3}, $Y_{C,chem} = 0.01$.
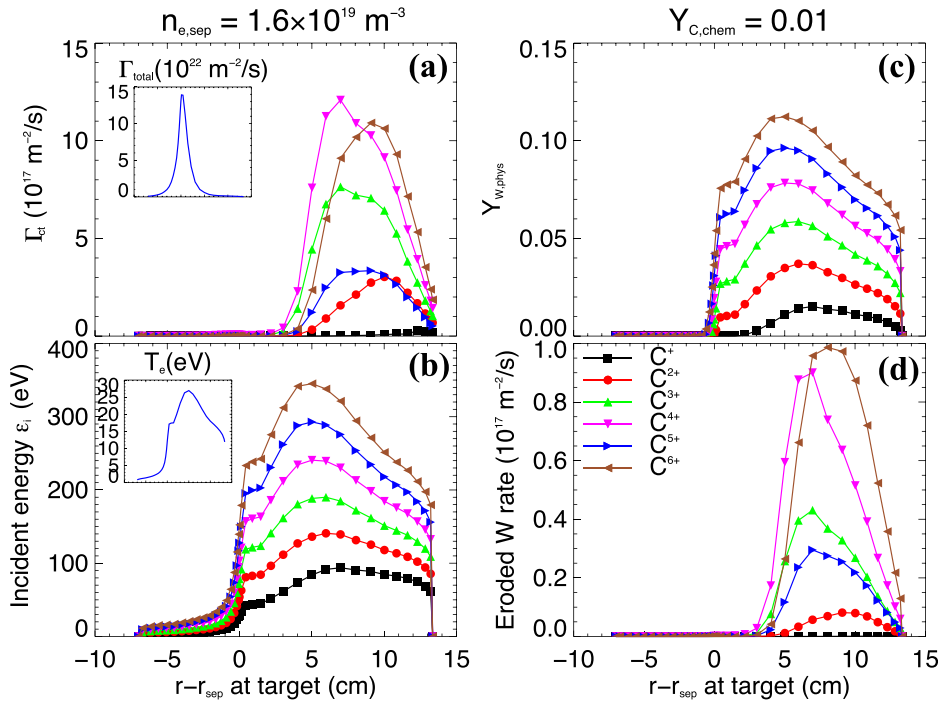
FIG. 8. The (a) particle flux density of each C ion (the inset-graph is the total particle flux density); (b) the averaged incident energy of each C ion (the inset-graph is the T_e); (c) the calculated W physical sputtering yield by each C ion; (d) the calculated W erosion rate by each C ion, at the UOT.

such as ERO,[22] EPPIC,[36] WBC,[76] and EDDY,[77] have been applied to study the local erosion of W by C. The DIVIMP code has been coupled with EDGE2D/EIRENE or B2-EIRENE (SOLPS) to calculate the W transport in the SOL of JET, USDEX Upgrade, and ITER.[78–80] Further works have been done by coupling the WallDYN code to DIVIMP to simulate wall erosion, global impurity migration, and redeposition.[81,82] In this work, the global C impurities transport and distribute, and the resulting W erosion is expected to be simulated. To roughly assess the W erosion by C in our cases, Yamamura's empirical formula,[83] which is a function of incident particle energy and angle, is applied to calculate the physical sputtering yield of W ($Y_{W,phys}$) by C. Since the gyromotion of the ions is not simulated by SOLPS, according to our experiences on ERO simulation of both EAST[84] and DIII-D wall erosion,[22] an averaged incidence angle of 45° is assumed in the calculations. The eroded W atom flux density can be calculated by $\Gamma_W = \Gamma_C Y_{W,phys}$, where the incident C flux density Γ_C is taken from the SOLPS output. As an example, Fig. 8 shows the incident flux density and averaged incident energy of each C ion species to the W UOT, for the case of $n_{e,sep}^{OMP} = 1.6 \times 10^{19}$ m^{-3}. It can be seen that the incident C ion flux density is about 10^{18} m^{-2} s^{-1}, five orders of magnitude lower than that of the total particle flux density [inset graph of Fig. 8(a)]. Due to the plasma sheath acceleration, higher charge state ions have higher incident energy. The peak T_e at the target is about 27 eV, as shown in Fig. 8(b), whereas the peak incident energy of C^{6+} could be as high as about 350 eV. The W physical sputtering yield and eroded flux by different C ions are shown in Figs. 8(c) and 8(d), respectively. It can be seen that the W physical sputtering yield by C^{6+} is the highest due to its highest incident energy. The highest eroded W flux densities are due to C^{4+} and C^{6+} incidence.

The total W erosion rate by C impurities at the UOT can be calculated by summing all the C species as shown in Fig. 8(d). Figure 9(a) shows the total eroded W flux distribution
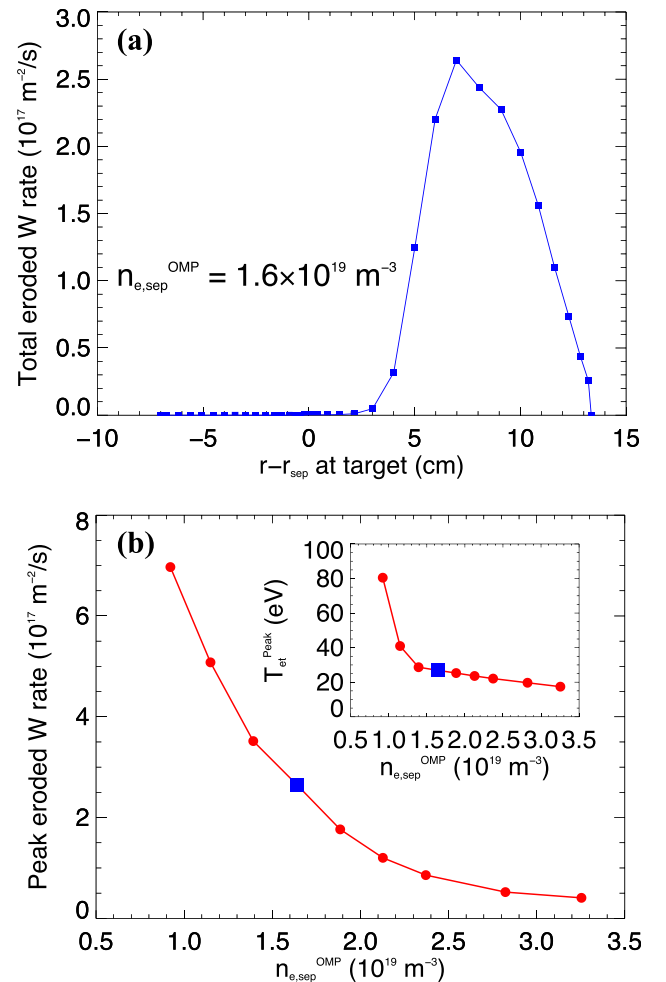

FIG. 9. The (a) profiles of the total W erosion rate by all C species at the UOT for the density $n_{e,sep}^{OMP} = 1.6 \times 10^{19}$ m^{-3}, (b) peak W erosion rate at the UOT as a function of $n_{e,sep}^{OMP}$, the blue point represents the peak values of (a), and the inset-graph is the corresponding peak T_e as a function of $n_{e,sep}^{OMP}$.
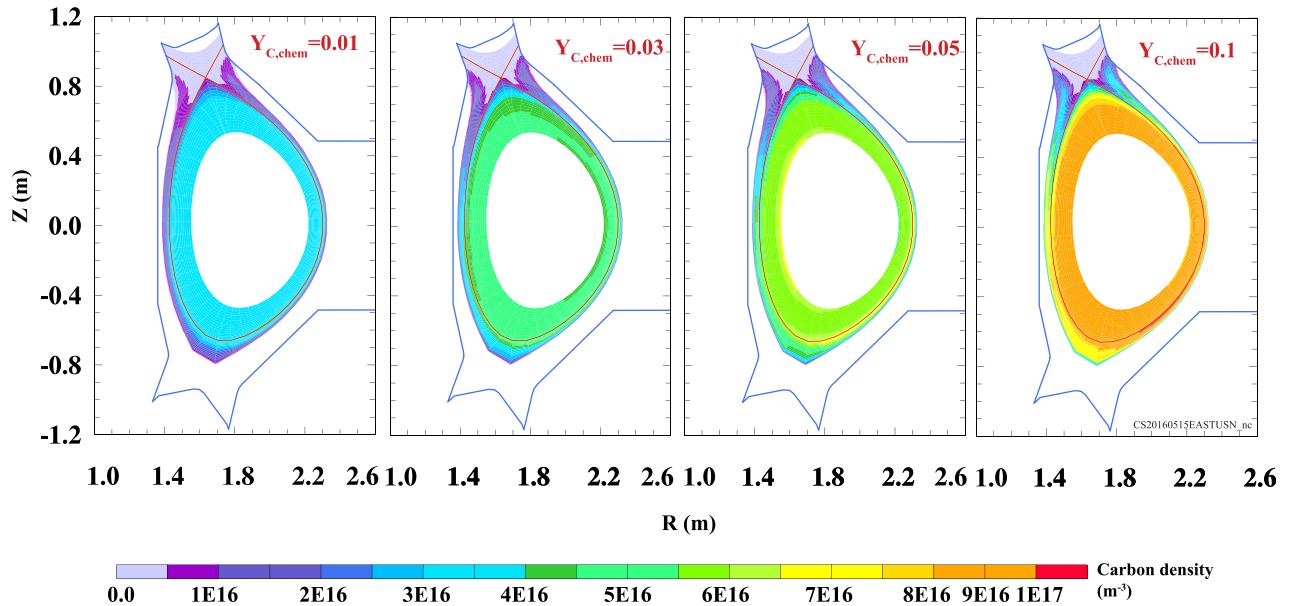
FIG. 10. The 2D contours of n_c with different $Y_{C,chem}$ (0.01, 0.05, 0.1).

along the UOT. The peak erosion rate is about 2.7×10^{17} W atoms m^{-2} s^{-1} and located far from the strike point (about r-r$_{sep}$ = 7 cm at target). Figure 9(b) shows the peak W erosion rate at the UOT as a function of $n_{e,sep}^{OMP}$. It can be seen that as $n_{e,sep}^{OMP}$ increases from 0.9×10^{19} to 3.3×10^{19} m^{-3}, the peak W erosion rate reduces from 7.0×10^{17} to 4.0×10^{16} W atoms m^{-2} s^{-1}. This agrees qualitatively with the experiments of ASDEX Upgrade.[85] The eroded W rate is a function of both incident ion energy and flux density. As the upstream density increases, the peak T$_e$ falls significantly, from 85 eV to 20 eV, which indicates that the incident averaged ion energy is also reduced. Meanwhile, the peak C flux density at the target is also suppressed by increasing $n_{e,sep}^{OMP}$, as indicated in Fig. 7(a). Both factors result in the reduction of the W erosion rate. It has been pointed out that in order to obtain reactor-relevant divertor conditions in a tokamak, T$_e$ should be below 5 eV to eliminate the W erosion by impurities.[5,7,86] In the low density case, since T$_e$ is over 80 eV, the W sputtering due to deuterium may become important, which is not included in the present estimation.

The above results indicate that the influence of C impurities on W erosion and the plasma solution (both upstream and downstream) is not significant for the low C source case ($Y_{C,chem} = 0.01$), USN configuration. Figure 10 shows the total carbon density distribution in the simulation domain with different $Y_{C,chem}$. It can be seen that as the C source is enhanced, the C density n_c increases significantly. However, C impurities still hardly reach the strike points and private flux regions. Moreover, n_c is much lower than the main plasma density (C concentration < 1%); thus, C impurities have very limited impact on the plasma performance even when $Y_{C,chem}$ is as high as 0.1. Figure 11 presents the peak W erosion rate at the UOT as a function of $Y_{C,chem}$. It is shown that the peak W erosion rate increases from 2.6×10^{17} to 8.1×10^{17} W atoms m^{-2} s^{-1}. While $Y_{C,chem}$ increases, the peak T$_e$ at the target remains almost the same, about 27 eV. The main reason for the W erosion rate

increment is the larger n_c at the UOT. We can see that the peak n_c increases from 3.7×10^{15} m^{-3} to 1.3×10^{16} m^{-3}, as shown in Fig. 11. Although the W erosion rate increases significantly when the C source is increased, the peak erosion is still smaller compared to the observation of DiMES experiments on DIII-D ($\sim 10^{18}$–10^{19} W atoms m^{-2} s^{-1}),[87,88] which is mainly due to different C concentrations. As it can be seen in Fig. 1, the C source is far from the upper target, and there is no plasma directly contacting the C wall in this USN simulation (Fig. 2). Therefore, n_c is very low in the simulation domain, especially in the upper divertor region. This indicates that the lower C divertor does not represent a big threat to the upper W divertor erosion for the USN operations.

C. The double null case

In this subsection, the DN case is simulated, as the computational mesh shown in Fig. 2. First, $Y_{C,chem}$ is fixed to
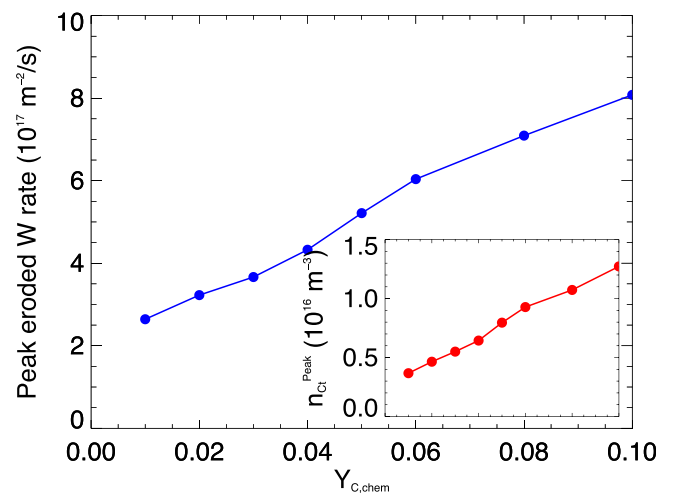

FIG. 11. The peak W erosion rate at the UOT as a function of $Y_{C,chem}$ and the inset-graph is the corresponding peak n_c at the UOT as a function of $Y_{C,chem}$.
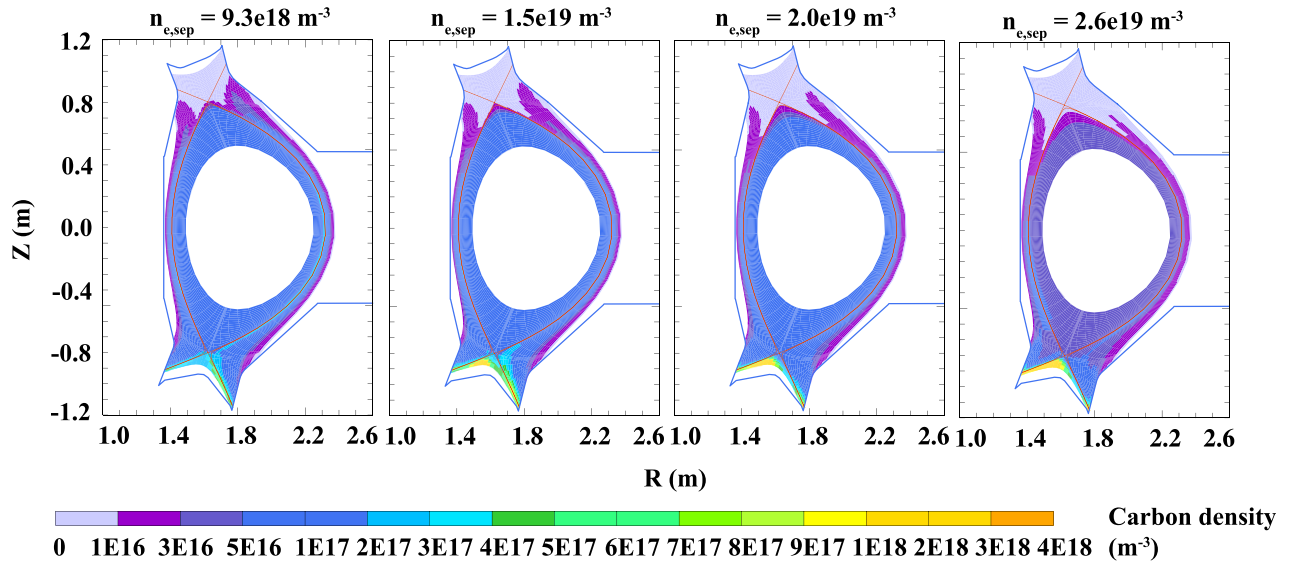
FIG. 12. The 2D contours of n_c with different $n_{e,sep}^{OMP}$ (9.3×10^{18} m^{-3}, 1.5×10^{19} m^{-3}, 2.0×10^{19} m^{-3}, 2.6×10^{19} m^{-3}).

0.01, and density scan is carried out. As expected, the T_{et} and q_t at the outer targets (both upper and lower) fall significantly as the $n_{e,sep}^{OMP}$ increases (not shown). The total carbon density distributions in the simulation domain with different $n_{e,sep}^{OMP}$ are shown in Fig. 12. It can be seen that most of the C impurities are accumulated in the lower divertor region, where they are produced. As the upstream density increases, n_c at the lower divertor increases significantly, mainly due to the enhanced incident particle fluxes to the lower target. However, n_c decreases with increasing $n_{e,sep}^{OMP}$ outside the lower target. The C impurities can hardly reach the upper divertor target, and the peak n_c values at the upper outer target reduce from 1.2×10^{16} m^{-3} to 3.5×10^{15} m^{-3} as $n_{e,sep}^{OMP}$ increases from 9.3×10^{18} m^{-3} to 2.6×10^{19} m^{-3}. This indicates that the transport of C above the lower X-point is also suppressed when T_e is low, similar to the USN case. As

$n_{e,sep}^{OMP}$ increases, the peak n_c location shifts to the lower inner divertor region, which is similar to the LSN case. It should be noted that the DN equilibrium used is a disconnected double null (DDN) equilibrium (dRsep $\neq$ 0), which has the main X-point at the bottom.

The radiated power as a function of $n_{e,sep}^{OMP}$ is shown in Fig. 13. The simulation domain is divided into three parts: (1) core+SOL, the region between the lower and upper X-points, (2) lower divertor, the region below the lower X-point, and (3) upper divertor, the region above the upper X-point, as shown in Fig. 2. It can be seen that C plays an important role in the total radiated power. C contributes more than 70% of the radiated power in the lower divertor due to its accumulation there. The fraction of C radiation power in the core+SOL region is smaller than 57%. In the upper divertor region, the proportion is less than 1% of the radiated power.
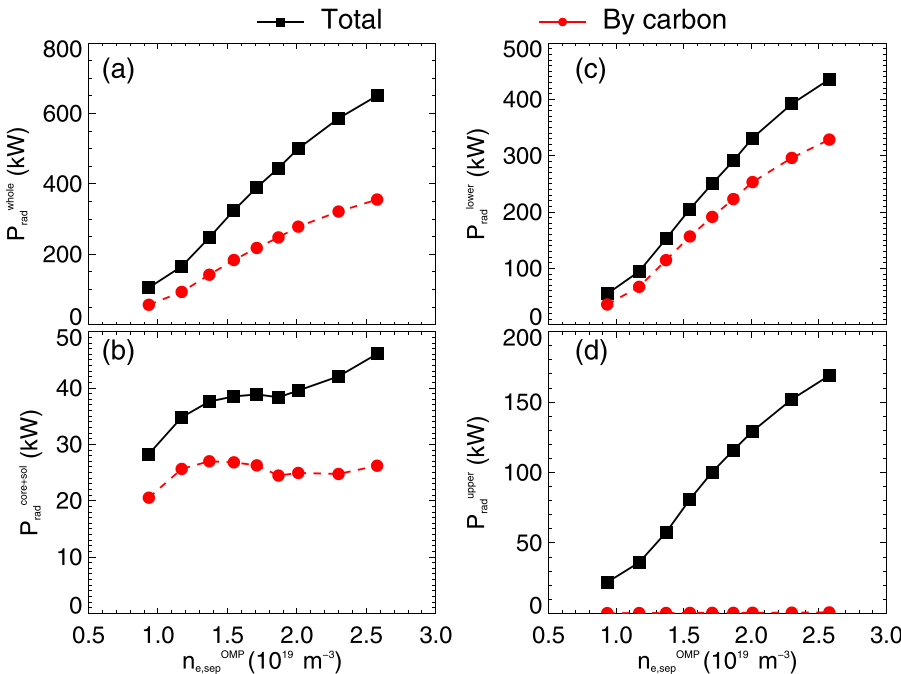

FIG. 13. The total and carbon radiated power in the (a) total simulation domain, (b) core and SOL region, (c) the lower divertor region, and (d) the upper divertor region, as functions of $n_{e,sep}^{OMP}$.
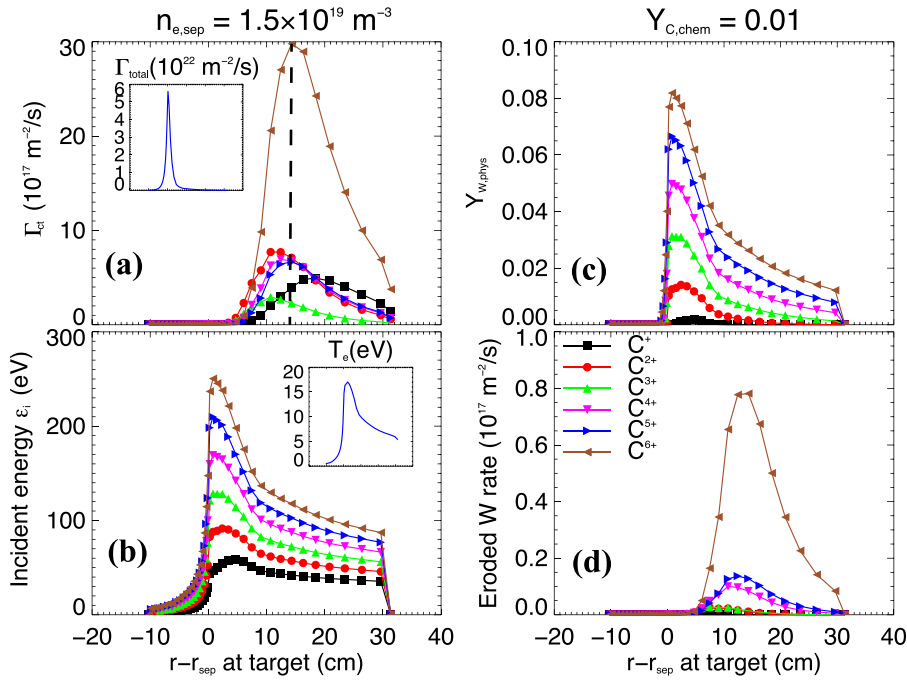
FIG. 14. The (a) particle flux density of each C ion (the inset-graph is the total particle flux density); (b) the averaged incident energy of each C ion (the inset-graph is T_e); (c) the calculated W physical sputtering yield by each C ion; (d) the calculated W erosion rate by each C ion, at the UOT.

This is understandable according to the C density distributions shown in Fig. 12. The lower divertor contributes most of the total radiated power from 52% to 67%, especially for the high density case. In this magnetic configuration, the main X-point of this DN is the lower one. Therefore, more power enters the lower divertor region than the upper divertor.

We use the same method as used for USN (Fig. 8) to calculate the W erosion rate at the UOT. The incident flux density, averaged incident energy, W sputtering yield, and W erosion rate, by different C ion species, for the density $n_{e,sep}^{OMP} = 1.5 \times 10^{19}$ m^{-3} are shown in Fig. 14. It can be seen that the incident C flux density ($\sim 10^{18}$ m^{-2} s^{-1}) is much smaller than the total incident flux density ($\sim 10^{22}$ m^{-2} s^{-1}). Moreover, the simulation indicates that for this geometry, the C^{6+} has higher flux than C ions of other charge states. The peak T_e at the UOT is about 17.5 eV, whereas the averaged C^{6+} incident energy could reach as high as 260 eV, resulting in the peak W physical erosion yield $Y_{W,phys} = 0.085$ by C^{6+}. Since C^{6+} has the largest incident flux and $Y_{W,phys}$, W erosion is predicted to be dominated by C^{6+}. It is worth noting that the peak averaged ion incident energy as well as T_e appears near the strike point location (within 1 cm), whereas the peak particle flux is located far away from the strike point (~ 14 cm). Such characteristics could help to reduce the total W erosion rate.

It appears that the C^{6+} dominates W erosion mainly due to its highest flux density, as shown in Fig. 14(a) for the DN geometry. To find out the reason, the flux tube, which contains the peak C^{6+} flux, is analyzed, as the dashed line shown in Fig. 14(a). Figure 15 shows the predicted poloidal particle flux density and particle density of each C ion species along the selected flux tube as a function of poloidal location. For C^{6+}, we can see that the peak density is located near the OMP, whereas the particle flux is the lowest. This indicates that most of the C^{6+} ions are from the core. The C impurities

are produced at the lower target, part of them transport along the flux tube (i.e., in the SOL or private region), and the other part of them would transport across the flux tube, entering into core plasma, where most of them would be ionized to the highest charge state C^{6+}. The OMP separatrix T_e is about 138 eV, which is too low to ionize C ions to C^{6+}. This again indicates that C^{6+} appearing outside the separatrix are
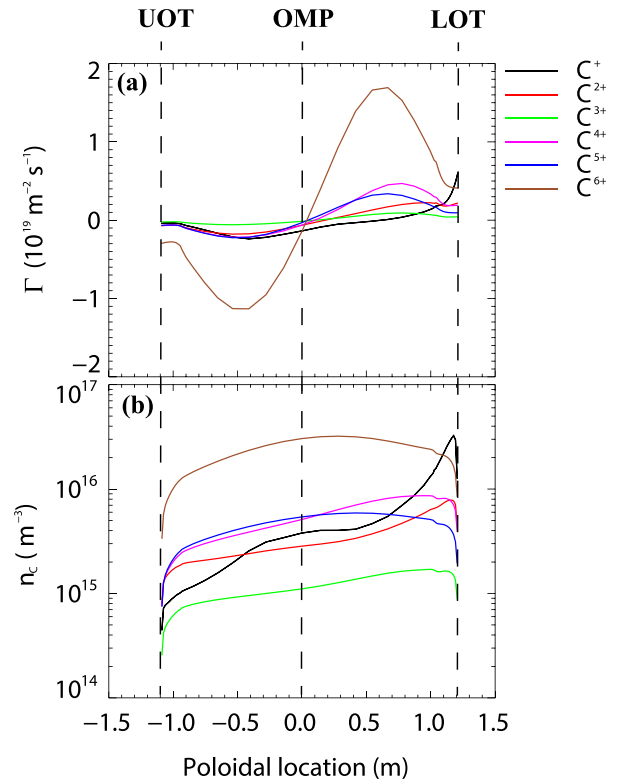

FIG. 15. The (a) poloidal particle flux density and (b) particle density, of each C charge state, along the flux tube shown in Fig. 14(a) (where the highest C^{6+} density exists at the UOT). The direction of the particle flux is from the UOT to the LOT.
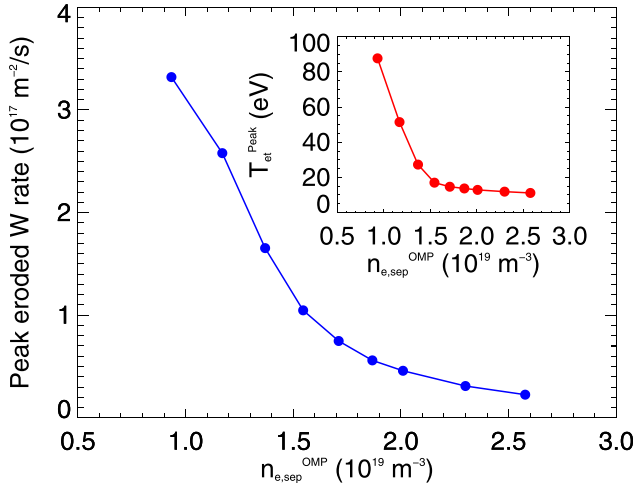
FIG. 16. The peak W erosion rate at the UOT as a function of $n_{e,sep}^{OMP}$, the inset-graph is the corresponding peak T_e as a function of $n_{e,sep}^{OMP}$.

transported from the core to the SOL. From Figs. 12 and 15, we can see that the cross-field transport plays an important role on the C impurity leaking from the lower divertor. For the lowest charged state, C^+, the peak density is located at the LOT, and the lowest density appears at the UOT. This means that C^+ ions mainly transport along the flux tube, from the LOT to the UOT.

We can see in Fig. 16 that the peak W erosion rate reduces significantly from 3.3×10^{17} to 2.3×10^{16} W atoms m^{-2} s^{-1}, as $n_{e,sep}^{OMP}$ increases from 9.3×10^{18} m^{-3} to 2.6×10^{19} m^{-3}. One reason is that the peak T_e is dropped from 88 eV to 11 eV. The other reason is the suppression of C impurity transport to the UOT as $n_{e,sep}^{OMP}$ increases, see Fig. 14. For the similar upstream density, the W erosion rate is even lower in the DN case compared to the USN case, as shown in Fig. 9(b). One reason is the different locations of peak incident C flux and peak incident C ion energy for the DN case, see Fig. 14. The other reason may be that, for this DN geometry, the lower X-point is the main X-point, and more particles are transported to the lower targets than to the upper targets. Therefore, particle flux to the upper targets is smaller than to those of the USN geometry case for the similar upstream plasma condition, see Figs. 8(a) and 14(a) the inset-graph of total incident flux. As a result, the peak W erosion rate is only about half of the USN case.

Figure 17 shows the total C density and electron temperature distribution in the whole simulation domain, with $n_{e,sep}^{OMP} = 1.5 \times 10^{19}$ m^{-3} for $Y_{C,chem} = 0.01, 0.03, 0.05, 0.1$. It can be seen that n_c is greatly increased with higher $Y_{C,chem}$. n_c at the LOT increases from 1.3×10^{18} m^{-3} to 1.3×10^{19} m^{-3}, from 1.6×10^{17} m^{-3} to 2.9×10^{17} m^{-3} at the OMP, and from 6.4×10^{15} m^{-3} to 3.2×10^{16} m^{-3} at the UOT. From the T_e
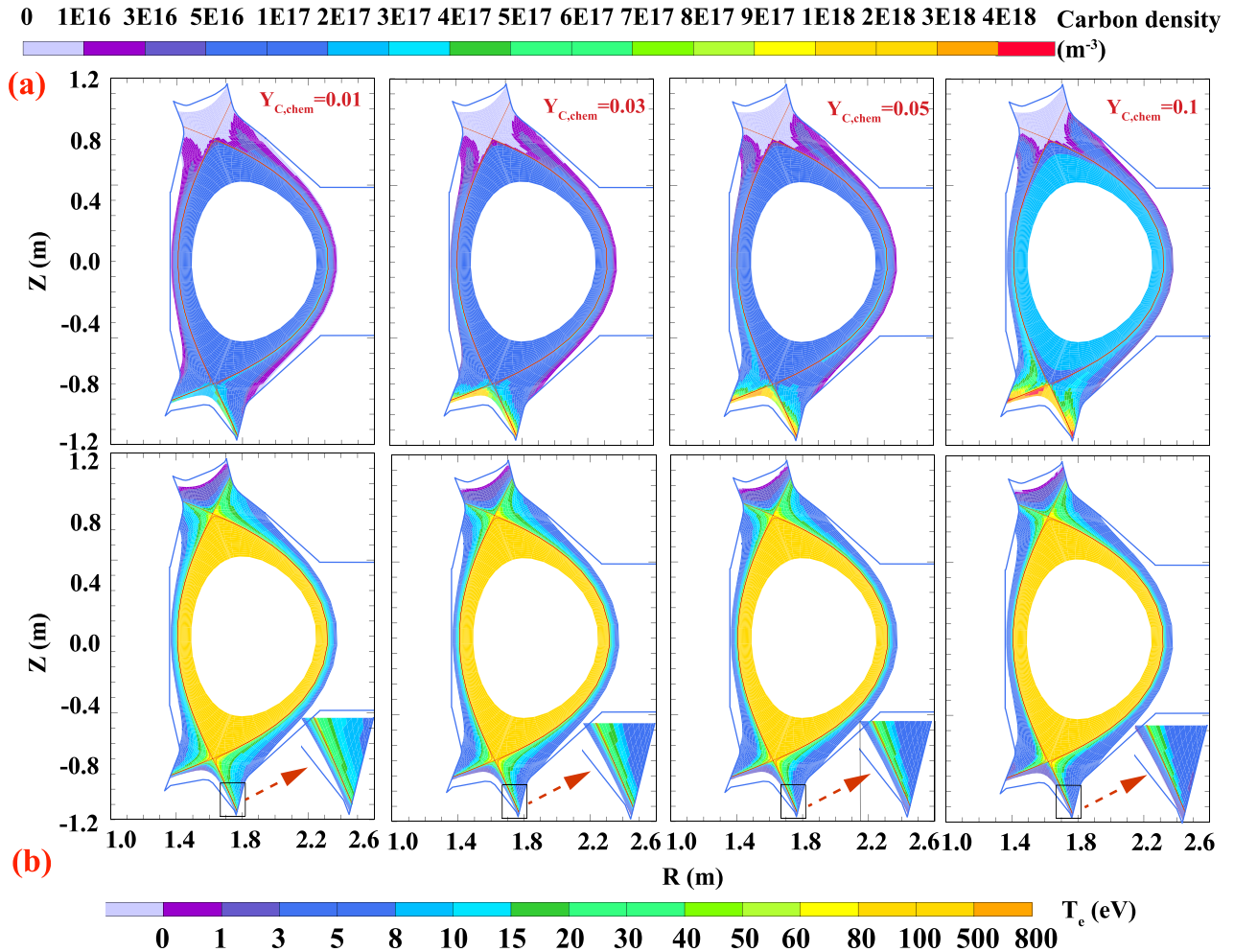

FIG. 17. The 2D contours of (a) n_c and (b) T_e. $Y_{C,chem} = 0.01, 0.03, 0.05, 0.1$.

distribution, we can see that the C impurities change the lower target plasma significantly, as shown in the close-up graphs in Fig. 17(b). The peak T_e at the LOT is reduced from 32.2 eV to 4.6 eV, similar to that of the LSN case; while the plasma condition at the UOT remains almost unchanged, similar to that of the USN case. The total radiated power contributed by C increases from 57% to 85%, and the lower divertor contributes most of the power radiation.

The effect of the C source at the lower target on the erosion of the upper W target is also studied. Figure 18 shows the peak W erosion rate at the UOT as a function of $Y_{C,chem}$. It can be seen that the peak W erosion rate increases from 1.0×10^{17} to 2.3×10^{17} W atoms m^{-2} s^{-1} as $Y_{C,chem}$ increases from 0.01 to 0.1. Since the peak T_e at the UOT remains almost unchanged (about 17 eV), the W erosion is mainly determined by the raising C incident flux. However, since it is difficult for C impurities to reach the upper divertor, as shown in Fig. 17(a), the W erosion rate is still low even when $Y_{C,chem} = 0.1$. In the simulation, a low input power 1.5 MW is applied. To study the performance of W erosion under high input power conditions, a power scan has been done, with assuming $Y_{C,chem} = 0.01$, $n_{e,sep}^{OMP} \sim 1.5 \times 10^{19}$ m^{-3}. Figure 19 shows the peak W eroded rate and peak T_e at the UOT as a function of P_{SOL} (1.5–4 MW). We can see that the W erosion rate increases by one order of magnitude, from 1.0×10^{17} to 1.1×10^{18} W atoms m^{-2} s^{-1}. The main reason is that the peak T_e increases from 17 eV to 75 eV, indicating that the averaged incident ion energy is also increased greatly. This proves that the input power is the other key parameter for the W erosion. We should note that when the peak T_e at the UOT reaches 75 eV ($P_{SOL} = 4$ MW), the averaged incident D$^+$ can reach as high as 236 eV, very close to the W sputtering threshold by D$^+$. In this condition, the W erosion by D$^+$ could be a big issue due to the large D$^+$ incident flux.[1,25,89,90] Therefore, a new operation scheme should be developed under high input power conditions to avoid the potential strong W erosion. Moreover, even though the averaged incident D$^+$ energy is well below the W sputtering threshold, there should be a small part of high energy
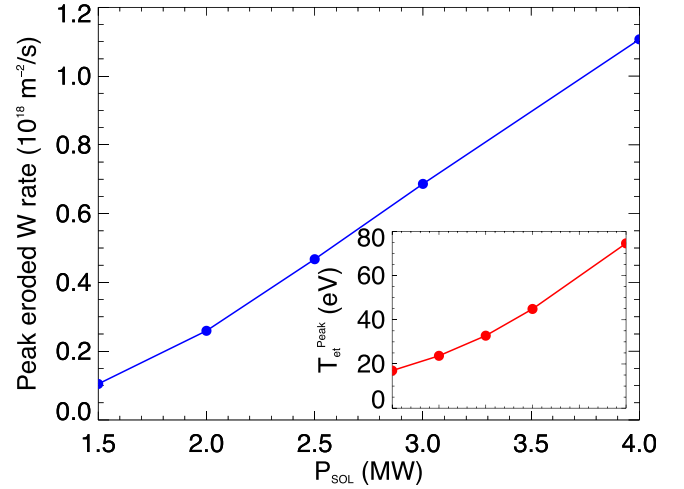
FIG. 19. The peak W erosion rate at the UOT as a function of the input power P_{SOL}, the inset-graph is the corresponding peak T_e along the UOT as a function of P_{SOL}.

D$^+$ particles, which could erode the W target. In this study, we consider only the averaged incident energy of each species. Monte Carlo/kinetic models, such as ERO and particle-in-cell, could take the incident particle energy distribution into consideration[22,36] so that we can calculate the W erosion rate more accurately. In addition, we should be aware that the transient off-normal events, such as ELMs, may make the W erosion issue much worse.[23,26] Moreover, the D$^+$ may become to a more important contributor to the W sources than other impurities during ELMs.[25,26]

IV. DISCUSSION AND CONCLUSIONS

Simulations have been done using the SOLPS5.0/EIRENE99 code package to study the transport of carbon impurities and its effects on the divertor plasma and tungsten erosion on EAST, which has both a graphite lower divertor target and tungsten upper divertor target simultaneously. The C impurity source is from the erosion of a lower graphite divertor target. Three typical magnetic field equilibrium configurations, i.e., LSN, USN, and DN, have been simulated. In the simulations, electrons and ions (D and C) at each ionization state are handled by the B2.5 code, while the neutrals (D, C, and D$_2$) are tracked by the EIRENE code. No W species have been simulated by SOLPS. The erosion rate of the W wall is calculated assuming a reasonable physical sputtering yield from the SOLPS output such as averaged incident ion energy and particle flux density of each species. These calculations are crude but effective to understand the global W erosion. From the simulations, it has been observed:

1. C is a good power radiator, which contributes to most of the radiated power for both LSN and DN configurations. The presence of C could help reduce the electron temperature and heat flux to the divertor target, as well as achieve detachment. These are in qualitative agreement with previous 2D fluid codes modelling of edge tokamak plasmas of carbon devices.[33,37,42,45,46,52,58,68–70,91] C favors to stay in the divertor regions, where it is produced. Therefore, the plasma condition above the lower X-point
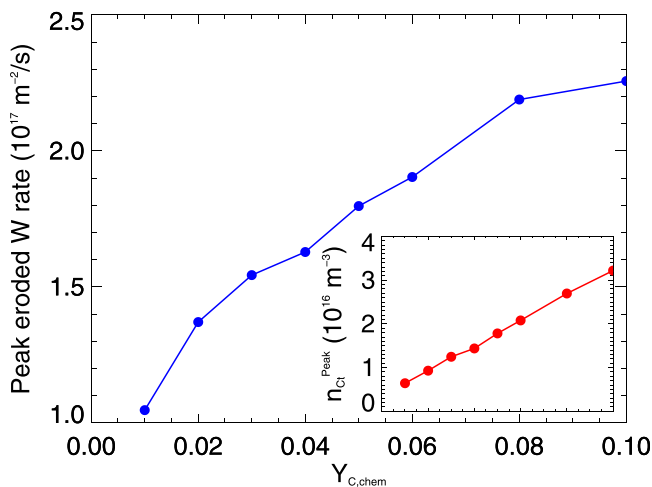

FIG. 18. The peak W erosion rate at the UOT as a function of $Y_{C,chem}$, the inset graph is the corresponding peak n_c along the UOT as a function of $Y_{C,chem}$.

has very small changes even when the C source strength is enhanced. Moreover, it is found that more C impurities accumulate on the lower inner leg region than the outer leg region, which is related to the divertor in-out asymmetry and the plasma pressure balance. The increase of the C source strength as well as increasing the upstream density could raise the C density significantly at the lower divertor and help to achieve plasma detachment. It should be noted that in the present simulations, the cross-field drifts[60,61,92] are not included. The drifts, especially $E \times B$ drifts, can redistribute plasma (drifts) flows significantly, see Refs. 52, 62, 63, 70, 93, and 94, thus affecting the W erosion rate. In further work, the effects of drifts on the W erosion should be addressed.

2. C impurities produced at the lower graphite target could reach the upper W targets and cause W erosion, for both USN and DN configurations. However, the concentration of the C density at the upper divertor is low, and thus, the W erosion rate by C impurities is very small (10^{17} -10^{18} W atoms m^{-2} s^{-1}) compared to the total incident particle density (10^{22}–10^{23} particles m^{-2} s^{-1}). Increasing the C source strength could raise the W erosion rate, whereas increasing the upstream plasma density may reduce the W erosion rate. For higher input powers, the erosion of W is enhanced greatly from 1.0×10^{17} ($P_{SOL} = 1.5$ MW) to 1.1×10^{18} ($P_{SOL} = 4$ MW) W atoms m^{-2} s^{-1}.

3. For the DN case, the W target is mainly eroded by C^{6+}, which is transported to the upper divertor through the core plasma, where most C ions are ionized to the highest charge state C^{6+}. Some C^{6+} ions are finally transported out of the separatrix and deposit either on the lower target or the upper target. At the upper divertor, the C^{6+} flux from the core is much more important than that of other C ions. Furthermore, it has the highest averaged incident energy, which leads to the highest W erosion. The impurity and charge state composition in the divertor are difficult to assess in experiment. Some Refs. 23, 24, and 85 assumed the C^{4+} to be the main impurity and calculated the W erosion flux by C^{4+} at a different level as a function of T_e, showing the agreement with the experimental measurement of ASDEX Upgrade. However, the carbon source location versus tungsten divertor in our simulation is different from that of USDEX Upgrade or JET.

By considering only the C impurities, the simulation results indicate that the upper W targets erosion rate by C is small on EAST, mainly due to the difficulties in C transport from lower divertor to the upper divertor region. We should keep in mind that due to the existence of other impurities such as Si and Li in EAST, the actual C sources and W erosion could be more complicated. The simulations show that when we increase the input power to 4 MW, the peak T_e at the upper target could reach 75 eV and the peak D^+ ion incident energy could be 236 eV, which may be a serious challenge due to the erosion of W by D^+ ions. EAST is continuing to upgrade its heating system to operate at higher power conditions. This requires reducing the peak T_e at the upper target to as low as possible. Impurity gas seeding, with, e.g., Ne, N_2, and Ar, is an alternative method to solve this problem. However, the introduced impurities may cause more erosion on the W divertor, which will need to be investigated in future work.

[1]G. Federici, C. H. Skinner, J. N. Brooks, J. P. Coad, C. Grisolia, A. A. Haasz, A. Hassanein, V. Philipps, C. S. Pitcher, J. Roth, W. R. Wampler, and D. G. Whyte, Nucl. Fusion **41**, 1967 (2001).

[2]R. A. Pitts, S. Carpentier, F. Escourbiac, T. Hirai, V. Komarov, A. S. Kukushkin, S. Lisgo, A. Loarte, M. Merola, R. Mitteau, A. R. Raffray, M. Shimada, and P. C. Stangeby, J. Nucl. Mater. **415**, S957 (2011).

[3]ITER Physics Expert Group on Divertor, Nucl. Fusion **39**, 2391 (1999).

[4]A. Loarte, B. Lipschultz, A. S. Kukushkin, G. Matthews, P. C. Stangeby, N. Asakura, G. F. Counsell, G. Federici, A. Kallenbach, K. Krieger, A. Mahdavi, V. Philipps, D. Reiter, J. Roth, J. Strachan, D. Whyte, R. Doerner, T. Eich, W. Fundamenski, A. Herrmann, M. Fenstermacher, P. Ghendrih, M. Groth, A. Kirschner, S. Konoshima, B. LaBombard, P. Lang, A. W. Leonard, P. Monier-Garbet, R. Neu, H. Pacher, B. Pegourie, R. A. Pitts, S. Takamura, J. Terry, and E. Tsitrone, Nucl. Fusion **47**, S203 (2007).

[5]W. Eckstein, "Calculated sputtering, reflection and range values," IPP Report No. IPP 9/132, 2002.

[6]G. Janeschitz, K. Borrass, G. Federici, Y. Igitkhanov, A. Kukushkin, H. D. Pacher, G. W. Pacher, and M. Sugihara, J. Nucl. Mater. **220–222**, 73 (1995).

[7]P. C. Stangeby and A. W. Leonard, Nucl. Fusion **51**, 063001 (2011).

[8]G. Federici, P. Andrew, P. Barabaschi, J. Brooks, R. Doerner, A. Geier, A. Herrmann, G. Janeschitz, K. Krieger, A. Kukushkin, A. Loarte, R. Neu, G. Saibene, M. Shimada, G. Strohmayer, M. Sugihara, and I. J. W. S. G. Cocenter, J. Nucl. Mater. **313–316**, 11 (2003).

[9]J. Roth and C. Garcia-Rosales, Nucl. Fusion **36**, 1647 (1996).

[10]T. Loarer, J. Nucl. Mater. **390–391**, 20 (2009).

[11]J. Roth, E. Tsitrone, T. Loarer, V. Philipps, S. Brezinsek, A. Loarte, G. F. Counsell, R. P. Doerner, K. Schmid, O. V. Ogorodnikova, and R. A. Causey, Plasma Phys. Controlled Fusion **50**, 103001 (2008).

[12]R. Causey, J. Nucl. Mater. **300**, 91 (2002).

[13]C. Sang, X. Bonnin, M. Warrier, A. Rai, R. Schneider, J. Sun, and D. Wang, Nucl. Fusion **52**, 043003 (2012).

[14]R. A. Pitts, S. Carpentier, F. Escourbiac, T. Hirai, V. Komarov, S. Lisgo, A. S. Kukushkin, A. Loarte, M. Merola, A. Sashala Naik, R. Mitteau, M. Sugihara, B. Bazylev, and P. C. Stangeby, J. Nucl. Mater. **438**, S48 (2013).

[15]B. Wan, S. Ding, J. Qian, G. Li, B. Xiao, and G. Xu, IEEE Trans. Plasma Sci. **42**, 495 (2014).

[16]A. M. Garofalo, V. S. Chan, J. M. Canik, M. E. Sawan, M. Choi, D. A. Humphreys, L. L. Lao, R. Prater, P. C. Stangeby, H. E. St. John, T. S. Taylor, A. D. Turnbull, and C. P. C. Wong, Nucl. Fusion **54**, 073015 (2014).

[17]G. Federici, R. Kemp, D. Ward, C. Bachmann, T. Franke, S. Gonzalez, C. Lowry, M. Gadomska, J. Harman, B. Meszaros, C. Morlock, F. Romanelli, and R. Wenninger, Fusion Eng. Des. **89**, 882 (2014).

[18]S. Brezinsek, T. Loarer, V. Philipps, H. G. Esser, S. Grünhagen, R. Smith, R. Felton, J. Banks, P. Belo, A. Boboc, J. Bucalossi, M. Clever, J. W. Coenen, I. Coffey, S. Devaux, D. Douai, M. Freisinger, D. Frigione, M. Groth, A. Huber, J. Hobirk, S. Jachmich, S. Knipe, K. Krieger, U. Kruezi, S. Marsen, G. F. Matthews, A. G. Meigs, F. Nave, I. Nunes, R. Neu, J. Roth, M. F. Stamp, S. Vartanian, and U. Samm, Nucl. Fusion **53**, 083023 (2013).

[19]V. Philipps, J. Nucl. Mater. **415**, S2 (2011).

[20]A. V. Chankin, D. P. Coster, and R. Dux, Plasma Phys. Controlled Fusion **56**, 025003 (2014).

[21]G. F. Matthews, J. Nucl. Mater. **438**, S2 (2013).

[22]R. Ding, P. C. Stangeby, D. L. Rudakov, J. D. Elder, D. Tskhakaya, W. R. Wampler, A. Kirschner, A. G. McLean, H. Y. Guo, V. S. Chan, and P. B. Snyder, Nucl. Fusion **56**, 016021 (2016).

[23]R. Dux, V. Bobkov, A. Herrmann, A. Janzer, A. Kallenbach, R. Neu, M. Mayer, H. W. Müller, R. Pugno, T. Pütterich, V. Rohde, and A. C. C. Sips, J. Nucl. Mater. **390–391**, 858 (2009).

[24]G. J. Van Rooij, J. W. Coenen, L. Aho-Mantila, S. Brezinsek, M. Clever, R. Dux, M. Groth, K. Krieger, S. Marsen, G. F. Matthews, A. Meigs, R. Neu, S. Potzel, T. Pütterich, J. Rapp, and M. F. Stamp, J. Nucl. Mater. **438**, S42 (2013).

[25]C. Guillemaut, A. Jardin, J. Horacek, I. Borodkina, A. Autricque, G. Arnoux, J. Boom, S. Brezinsek, J. W. Coenen, E. De La Luna, S. Devaux, T. Eich, D. Harting, A. Kirschner, B. Lipschultz, G. F. Matthews, A. Meigs, D. Moulton, M. O'Mullane, and M. Stamp, Phys. Scr. **T167**, 014005 (2016).

[26]N. Den Harder, S. Brezinsek, T. Pütterich, N. Fedorczak, G. F. Matthews, A. Meigs, M. F. Stamp, M. C. M. van de Sanden, and G. J. Van Rooij, Nucl. Fusion **56**, 026014 (2016).

[27]J. Li, H. Y. Guo, B. N. Wan, X. Z. Gong, Y. F. Liang, G. S. Xu, K. F. Gan, J. S. Hu, H. Q. Wang, L. Wang, L. Zeng, Y. P. Zhao, P. Denner, G. L. Jackson, A. Loarte, R. Maingi, J. E. Menard, M. Rack, and X. L. Zou, Nat. Phys. **9**, 817 (2013).

[28]Y. Chen, Z. Wu, W. Gao, L. Zhang, Y. Jie, J. Zhang, Q. Zang, J. Huang, G. Zuo, and J. Zhao, Plasma Phys. Controlled Fusion **56**, 105006 (2014).

[29]B. Wan, J. Li, H. Guo, Y. Liang, G. Xu, L. Wang, X. Gong, and A. Garofalo, Nucl. Fusion **55**, 104015 (2015).

[30]J. G. Li, G. N. Luo, R. Ding, D. M. Yao, J. L. Chen, L. Cao, J. S. Hu, and Q. Li, Phys. Scr. **T159**, 014001 (2014).

[31]D. M. Yao, G. N. Luo, Z. B. Zhou, L. Cao, Q. Li, W. J. Wang, L. Li, S. G. Qin, Y. L. Shi, G. H. Liu, and J. G. Li, Phys. Scr. **T167**, 014003 (2016).

[32]D. Yao, G. Luo, S. Du, L. Cao, Z. Zhou, T. Xu, X. Ji, C. Liu, C. Liang, Q. Li, W. Wang, S. Zhao, Y. Xu, L. Li, Z. Wang, X. X. M. Qi, S. Wang, and J. Li, Fusion Eng. Des. **98–99**, 1692 (2015).

[33]M. Wischmeier, X. Bonnin, D. P. Coster, A. V. Chankin, A. Kallenbach, and H. W. Müller, Contrib. Plasma Phys. **48**, 249 (2008).

[34]H. Y. Guo, S. Zhu, and J. Li, J. Nucl. Mater. **363–365**, 162 (2007).

[35]B. Lipschultz, X. Bonnin, G. Counsell, A. Kallenbach, A. Kukushkin, K. Krieger, A. Leonard, A. Loarte, R. Neu, R. A. Pitts, T. Rognlien, J. Roth, C. Skinner, J. L. Terry, E. Tsitrone, D. Whyte, S. Zweben, and N. Asakura, Nucl. Fusion **47**, 1189 (2007).

[36]Z. Sun, C. Sang, W. Hu, H. Du, and D. Wang, Fusion Eng. Des. **109–111**, 213 (2016).

[37]A. V. Chankin, D. P. Coster, R. Dux, C. Fuchs, G. Haas, A. Herrmann, L. D. Horton, A. Kallenbach, B. Kurzan, H. W. Müller, R. Pugno, M. Wischmeier, and E. Wolfrum, Nucl. Fusion **49**, 015004 (2009).

[38]N. Asakura, K. Shimizu, K. Hoshino, K. Tobita, S. Tokunaga, and T. Takizuka, Nucl. Fusion **53**, 123013 (2013).

[39]M. Wischmeier, R. A. Pitts, A. Alfier, Y. Andrehe, R. Behn, D. Coster, J. Horacek, P. Nielsen, R. Pasqualotto, D. Reiter, and A. Zabolotsky, Contrib. Plasma Phys. **44**, 268 (2004).

[40]A. S. Kukushkin, H. D. Pacher, A. Loarte, V. Komarov, V. Kotov, M. Merola, G. W. Pacher, and D. Reiter, Nucl. Fusion **49**, 075008 (2009).

[41]C. Sang, H. Du, G. Zuo, X. Bonnin, J. Sun, L. Wang, and D. Wang, Nucl. Fusion **56**, 106018 (2016).

[42]A. E. Jaervinen, C. Giroud, M. Groth, P. Belo, S. Brezinsek, M. Beurskens, G. Corrigan, S. Devaux, P. Drewelow, D. Harting, A. Huber, S. Jachmich, K. Lawson, B. Lipschultz, G. Maddison, C. Maggi, C. Marchetto, S. Marsen, G. F. Matthews, A. G. Meigs, D. Moulton, B. Sieglin, M. F. Stamp, and S. Wiesen, Nucl. Fusion **56**, 046012 (2016).

[43]H. L. Du, C. F. Sang, L. Wang, X. Bonnin, H. Y. Guo, J. Z. Sun, and D. Z. Wang, Plasma Phys. Controlled Fusion **58**, 085006 (2016).

[44]V. Kotov, D. Reiter, R. A. Pitts, S. Jachmich, A. Huber, and D. P. Coster, Plasma Phys. Controlled Fusion **50**, 105012 (2008).

[45]J. M. Canik, A. R. Briesemeister, C. J. Lasnier, A. W. Leonard, J. D. Lore, A. G. McLean, and J. G. Watkins, J. Nucl. Mater. **463**, 569 (2015).

[46]E. Havlíčková, J. Harrison, B. Lipschultz, G. Fishpool, A. Kirk, A. Thornton, M. Wischmeier, S. Elmore, and S. Allan, Plasma Phys. Controlled Fusion **57**, 115001 (2015).

[47]F. Reimold, M. Wischmeier, M. Bernert, S. Potzel, D. Coster, X. Bonnin, D. Reiter, G. Meisl, A. Kallenbach, L. Aho-Mantila, and U. Stroth, J. Nucl. Mater. **463**, 128 (2015).

[48]R. Schneider, X. Bonnin, K. Borrass, D. P. Coster, H. Kastelewicz, D. Reiter, V. A. Rozhansky, and B. J. Braams, Contrib. Plasma Phys. **46**, 3 (2006).

[49]D. Reiter, The EIRENE Code User Manual Version: 11/2009, 2009.

[50]D. Reiter, M. Baelmans, and P. Börner, Fusion Sci. Technol. **47**, 172 (2005).

[51]M. Chang, C. Sang, Z. Sun, W. Hu, and D. Wang, Phys. Plasmas **25**, 052507 (2018).

[52]G. D. Porter, T. W. Petrie, T. D. Rognlien, and M. E. Rensink, Phys. Plasmas **17**, 112501 (2010).

[53]C. F. Sang, P. C. Stangeby, H. Y. Guo, A. W. Leonard, B. Covele, L. L. Lao, and D. M. Thomas, Plasma Phys. Controlled Fusion **59**, 025009 (2017).

[54]H. L. Du, C. F. Sang, L. Wang, X. Bonnin, J. Z. Sun, and D. Z. Wang, Fusion Eng. Des. **89**, 2461 (2014).

[55]X. Bonnin and D. Coster, J. Nucl. Mater. **415**, S488 (2011).

[56]D. P. Coster, A. V. Chankin, H.-J. Klingshirn, R. Dux, E. Fable, X. Bonnin, A. Kukushkin, and A. Loarte, J. Nucl. Mater. **463**, 620 (2015).

[57]L. L. Lao, H. St. John, R. D. Stambaugh, A. G. Kellman, and W. Pfeiffer, Nucl. Fusion **25**, 1611 (1985).

[58]A. V. Chankin, D. P. Coster, R. Dux, C. Fuchs, G. Haas, A. Herrmann, L. D. Horton, A. Kallenbach, M. Kaufmann, C. Konz, K. Lackner, C. Maggi, H. W. Muller, J. Neuhauser, R. Pugno, M. Reich, and W. Schneider, Plasma Phys. Controlled Fusion **48**, 839 (2006).

[59]Y. Chen, F. Q. Wang, X. J. Zha, L. Q. Hu, H. Y. Guo, Z. W. Wu, X. D. Zhang, B. N. Wan, and J. G. Li, Phys. Plasmas **20**, 022311 (2013).

[60]A. V. Chankin, J. Nucl. Mater. **241–243**, 199 (1997).

[61]P. C. Stangeby and A. V. Chankin, Nucl. Fusion **36**, 839 (1996).

[62]A. V. Chankin, G. Corrigan, M. Groth, and P. C. Stangeby, Plasma Phys. Controlled Fusion **57**, 095002 (2015).

[63]D. K. Morozov, V. A. Rozhansky, J. J. E. Herrera, and T. K. Soboleva, Phys. Plasmas **7**, 1184 (2000).

[64]F. Reimold, M. Wischmeier, M. Bernert, S. Potzel, A. Kallenbach, H. W. Müller, B. Sieglin, and U. Stroth, and the ASDEX Upgrade Team, Nucl. Fusion **55**, 33004 (2015).

[65]T. D. Rognlien, J. L. Milovich, M. E. Rensink, and G. D. Porter, J. Nucl. Mater. **196–198**, 347 (1992).

[66]R. Simonini, G. Corrigan, G. Radford, J. Spence, and A. Taroni, Contrib. Plasma Phys. **34**, 368 (1994).

[67]S. Wiesen, EDGE2D/EIRENE Code Interface Report, 2006.

[68]M. Groth, S. Brezinsek, P. Belo, M. N. A. Beurskens, M. Brix, M. Clever, J. W. Coenen, C. Corrigan, T. Eich, J. Flanagan, C. Guillemaut, C. Giroud, D. Harting, A. Huber, S. Jachmich, U. Kruezi, K. D. Lawson, M. Lehnen, C. Lowry, C. F. Maggi, S. Marsen, A. G. Meigs, R. A. Pitts, G. Sergienko, B. Sieglin, C. Silva, A. Sirinelli, M. F. Stamp, G. J. van Rooij, and S. Wiesen, and the JET-EFDA Contributors. Nucl. Fusion **53**, 093016 (2013).

[69]G. D. Porter, R. Isler, J. Boedo, and T. D. Rognlien, Phys. Plasmas **7**, 3663 (2000).

[70]M. Groth, G. D. Porter, M. E. Rensink, T. D. Rognlien, S. Wiesen, M. Wischmeier, T. Eich, A. Herrmann, S. Jachmich, C. J. Lasnier, H. W. Müller, J. G. Watkins, M. N. A. Beurskens, B. D. Bray, S. Brezinsek, N. H. Brooks, M. E. Fenstermacher, C. Fuchs, A. Huber, A. Kallenbach, A. W. Leonard, A. Meigs, and D. L. Rudakov, J. Nucl. Mater. **415**, S530 (2011).

[71]P. C. Stangeby, *The Plasma Boundary of Magnetic Fusion Devices* (Institute of Physics Publishing, Bristol, 2000).

[72]B. LaBombard, J. A. Goetz, C. Kurz, D. Jablonski, B. Lipschultz, G. M. McCracken, A. Niemczewski, R. L. Boivin, F. Bombarda, C. Christensen, S. Fairfax, C. Fiore, D. T. Garnier, M. A. Graf, S. N. Golovato, R. S. Granetz, M. J. Greenwald, S. F. Horne, A. E. Hubbard, I. H. Hutchinson, J. H. Irby, J. Kesner, T. LUKE, E. S. Marmar, M. J. May, P. OShea, M. Porkolab, J. Reardon, J. E. Rice, J. Schachter, J. A. Snipes, P. C. Stek, Y. Takase, J. L. Terry, G. TINIOS, R. L. Watterson, B. Welch, and S. M. Wolfe, Phys. Plasmas **2**, 2242 (1995).

[73]A. Loarte, R. D. Monk, J. R. Martín-Solís, D. J. Campbell, A. V. Chankin, S. Clement, S. J. Davies, J. Ehrenberg, S. K. Erents, H. Y. Guo, P. J. Harbour, L. D. Horton, L. C. Ingesson, H. Jäckel, J. Lingertat, C. G. Lowry, C. F. Maggi, G. F. Matthews, K. McCormick, D. P. O'Brien, R. Reichle, G. Saibene, R. J. Smith, M. F. Stamp, D. Stork, and G. C. Vlases, Nucl. Fusion **38**, 331 (1998).

[74]V. Kotov and D. Reiter, Plasma Phys. Controlled Fusion **51**, 115002 (2009).

[75]P. C. Stangeby, J. M. Canik, and D. G. Whyte, Nucl. Fusion **50**, 125003 (2010).

[76]J. N. Brooks, Fusion Eng. Des. **60**, 515 (2002).

[77]K. Ohya, Phys. Scr. **T124**, 70 (2006).

[78]A. Järvinen, C. Giroud, M. Groth, K. Krieger, D. Moulton, S. Wiesen, and S. Brezinsek, Phys. Scr. **T145**, 014013 (2011).

[79]A. Geier, K. Krieger, J. D. Elder, R. Pugno, and V. Rohde, J. Nucl. Mater. **313–316**, 1216 (2003).

[80]K. Schmid, K. Krieger, A. Kukushkin, and A. Loarte, J. Nucl. Mater. **363–365**, 674 (2007).

[81]K. Schmid, K. Krieger, S. W. Lisgo, G. Meisl, and S. Brezinsek, J. Nucl. Mater. **463**, 66 (2015).

[82]K. Schmid, K. Krieger, S. W. Lisgo, G. Meisl, and S. Brezinsek, Nucl. Fusion **55**, 53015 (2015).

[83]Y. Yamamura, Y. Itikawa, and N. Itoh, see http://Dpc.Nifs.Ac.Jp/IPPJ-AM/IPPJ-AM-List.Html for "Angular dependence of sputtering yields of monoatomic solids," 1983.

[84]R. Ding, R. A. Pitts, D. Borodin, S. Carpentier, F. Ding, X. Z. Gong, H. Y. Guo, A. Kirschner, M. Kocan, J. G. Li, G.-N. Luo, H. M. Mao, J. P. Qian, P. C. Stangeby, W. R. Wampler, H. Q. Wang, and W. Z. Wang, Nucl. Fusion **55**, 023013 (2015).

[85]K. Krieger, H. Maier, and R. Neu, J. Nucl. Mater. **266–269**, 207 (1999).

[86]W. Eckstein, Vacuum **82**, 930 (2008).

[87]T. Abrams, R. Ding, H. Y. Guo, A. W. Leonard, D. M. Thomas, A. G. Mclean, A. R. Briesemeister, M. Makowski, E. A. Unterberg, and C. Chrobak, in Proceedings of 22nd International Conference on Plasma Surface Interactions in Controlled Fusion Devices, Roma (2016).

[88]T. Abrams, R. Ding, H. Y. Guo, D. M. Thomas, C. P. Chrobak, D. L. Rudakov, A. G. McLean, E. A. Unterberg, A. R. Briesemeister, P. C. Stangeby, J. D. Elder, W. R. Wampler, and J. G. Watkins, Nucl. Fusion **57**, 056034 (2017).

[89]R. Neu, Plasma Phys. Controlled Fusion **53**, 124040 (2011).

[90]V. Philipps, R. Neu, J. Rapp, U. Samm, M. Tokar, T. Tanabe, and M. Rubel, Plasma Phys. Controlled Fusion **42**, B293 (2000).

[91]C. Sang, H. Y. Guo, P. C. Stangeby, L. L. Lao, and T. S. Taylor, Nucl. Fusion **57**, 056043 (2017).

[92]T. D. Rognlien, D. D. Ryutov, N. Mattor, and G. D. Porter, Phys. Plasmas **6**, 1851 (1999).

[93]J. A. Boedo, M. J. Schaffer, R. Maingi, and C. J. Lasnier, Phys. Plasmas **7**, 1075 (2000).

[94]L. Aho-Mantila, M. Wischmeier, K. Krieger, V. Rohde, H. W. Müller, D. P. Coster, M. Groth, A. Kirschner, R. Neu, S. Potzel, B. Sieglin, and E. Wolfrum, J. Nucl. Mater. **415**, S231 (2011).